Politecnico di Torino

Politecnico di Torino

Master's Degree in Nanotechnologies for ICT
Academic year 2024/25
Graduation session December 2025

Towards chipscale atomic clocks

Fabrication and characterization of Rubidium vapor microcells

Supervisors

Dott. Erik Cerrato
Dott. Michele Gozzelino
Prof. Marco Vacca

Candidate

Cesare Piemontese

Summary

The renewed interest in portable metrology equipment has led researchers towards the down-scaling of time and frequency standards, trying to retain the best possible performances. The effort is aimed at achieving a fundamental breakthrough in transportable applications, where minimizing the power consumption, volume, and size of quantum devices is essential. In this thesis, I present my work on the production and characterization of one of the main components of a portable atomic clock, namely the microcell containing the atomic vapors on which the clock interrogation is performed. To improve the clock performance in terms of stability and accuracy, the atoms interogation is based on two-photon Doppler-free spectroscopy at 778 nm. Microcell fabrication was carried out in cleanroom environment, inside of *PiQuET* facility, through the implementation of standard Silicon technology techniques mutuated from the microelectronics community, including, but not limited to, photolithographic processes on Silicon wafers, metal layers depositions and wafer bonding techniques. The quality of the cells was tested on a saturated absorption spectroscopy setup, and their performance in terms of signal intensity and linewidth was evaluated in the Doppler-free two-photon spectroscopy setup used to implement the atomic clock. The filling dynamics of the atomic vapors in the cells was studied and linked to their geometry and design choices. Optimization of the layouts, of the fabrication steps and recipes, and of the optical setups carried out during the experiments are also presented along with their impact on the results. The final outcome is a microcell with a state of the art performance in terms of signal-to-noise ratio and linewidth, showing great potential for the implementation of a compact and portable atomic clock based on two-photon spectroscopy.

Acknowledgements

"This work has been performed at the research infrastructure PiQuET (Piemonte Quantum Enabling Technologies), at INRiM, supported by Regione Piemonte".

Table of Contents

List of Tables

List of Figures

Acronyms

DRIE

Deep Reactive Ion Etching

PiQuET

Piemonte Quantum Enabling Technology

MEMS

Micro Electromechanical System

PR

Photoresist

VOA

Variable Optical Attenuator

OA

Optical Amplifier

PMT

Photomultiplier Tube

PD

Photodiode

SEM

Scanning Electron Microscope

2PS

Two-Photon spectroscopy

AS

Absorption Spectroscopy

ICP-RIE

Inductively Coupled Plasma - Reactive Ion Etching

CW

Continuous Wave

SHG

Second Harmonic Generation

LO

Local Oscillator

FWHM

Full Width at Half Maximum

SWaP

Size, Weight and Power

EDFA

Erbium Doped Fiber Amplifier

PPLN

Periodically Poled Lithium Niobate

CCD

Charge Coupled Device

Chapter 1

Introduction

Atomic frequency standards are devices that derive a stable frequency reference from well-defined atomic transitions by locking the frequency of a Local Oscillator (LO), usually a OXCA quartz crystal in the microwave range or a laser in the optical range, to the transition itself (**Figure 1.1**). When the frequency standards are

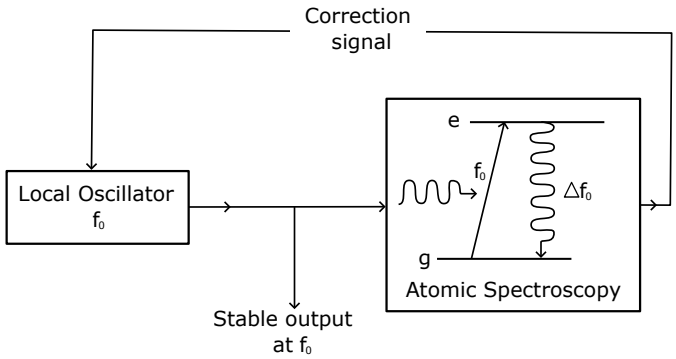

Figure 1.1: Schematic representation of a generic atomic frequency reference. The frequency of a local oscillator (LO) is locked to the frequency of an atomic transition using a feedback loop. The atomic reference provides a stable and accurate frequency standard, which is used to correct the LO frequency.

used to drive a counter, the resulting devices are called *atomic clocks*. The use of atomic transitions to create precise clocks dates back to 1945 when physicist Isador Rabi first proposed the idea [1]. Since then, atomic clocks have revolutionized timekeeping to unprecedented precision levels, to the point where the unit of time itself (the second) has been defined in terms of a specific number of Caesium oscillations in 1967 [2], which became the so-called *primary standard* of time:

> *"The second is the duration of 9 192 631 770 periods of the radiation corresponding to the transition between two hyperfine levels of the ground*

state of the Caesium-133 atom (at rest and in a null magnetic field).“

Such laboratory primary standards based on microwave hyperfine transitions have set international time scales for decades. In the continuous effort towards even more precise timekeeping devices, the frequency stability of a frequency standard plays an important role as a figure of merit, and is defined as:

$$\sigma_y(\tau) = \frac{1}{K}\frac{1}{Q}\frac{1}{S/N}\frac{1}{\sqrt{\tau/s}} \tag{1.1}$$

where K is a constant on the order of unity depending on the interrogation method, S/N is the signal-to-noise ratio of the spectroscopic signal, $Q = \nu_0/\Delta\nu$ is the quality factor of the atomic resonance (with ν_0 the transition frequency and $\Delta\nu$ its linewidth) and τ is the averaging time. It is evident how switching from microwave (GHz) to optical (THz) frequencies (with the same linewidth), or having a smaller linewidth (at the same frequency) provides an increase in the quality factor Q and thus a better frequency stability. Even though it is not obvious that the other parameters, such as S/N, can be kept to favourable values when changing to different atomic references and interrogation schemes, nowadays optical frequency standards have surpassed microwave clocks in performance (by almost 3 orders of magnitude [3]), so that even the redefinition of the second is being considered [4]. Parallel to their laboratory development as primary standards, there has been a growing demand for portable atomic clocks that can operate reliably outside controlled environments, for applications such as satellite navigation, telecommunications synchronization, deployed sensing, dark matter detection [5, 6] as well as tests on fundamental physics and general relativity [7, 8]. Portable atomic clocks aim to provide low Size, Weight, and Power (SWaP index [9]) while maintaining good stability over a wide range of timescales. Enabled by advances in lasers and optical frequency combs, also such portable clocks are increasingly based on optical transitions, which offer higher frequencies and narrower linewidths than microwave transitions, leading to improved stability and accuracy. The need for compact and robust systems that provide frequency stabilities of $\sim 10^{-13}$ at 1 s and approach 10^{-15} at day-long averaging, without the complexity of laser cooling or ultra-high vacuum, motivates the use of simpler architectures, such as warm-vapor optical clocks, as practical successors to commercial microwave devices [10].

1.1 Microfabricated vapor cells: toward compact, manufacturable clocks

Portable atomic clocks can be rack-scale (tens of liters, tens of watts), tabletop (hundreds of milliliters, a few watts), or chip-scale (few cubic centimeters, hundreds

of milliwatts). Commercial rack-scale vapor-cell optical clocks based on Rb two-photon interrogation now report long-term instabilities approaching a few $\times 10^{-15}$ at 10^4 s, while maintaining robust, automated operation [9]. Although such instruments are not yet "chip-scale," they demonstrate that warm-vapor, Doppler-free optical standards can reach performance levels that substantially exceed compact microwave Rb standards (typically $\sim 10^{-11}$ at 1 s), especially at medium-to-long averaging times. The first actual chip-scale clock was built in 2004 [12], and

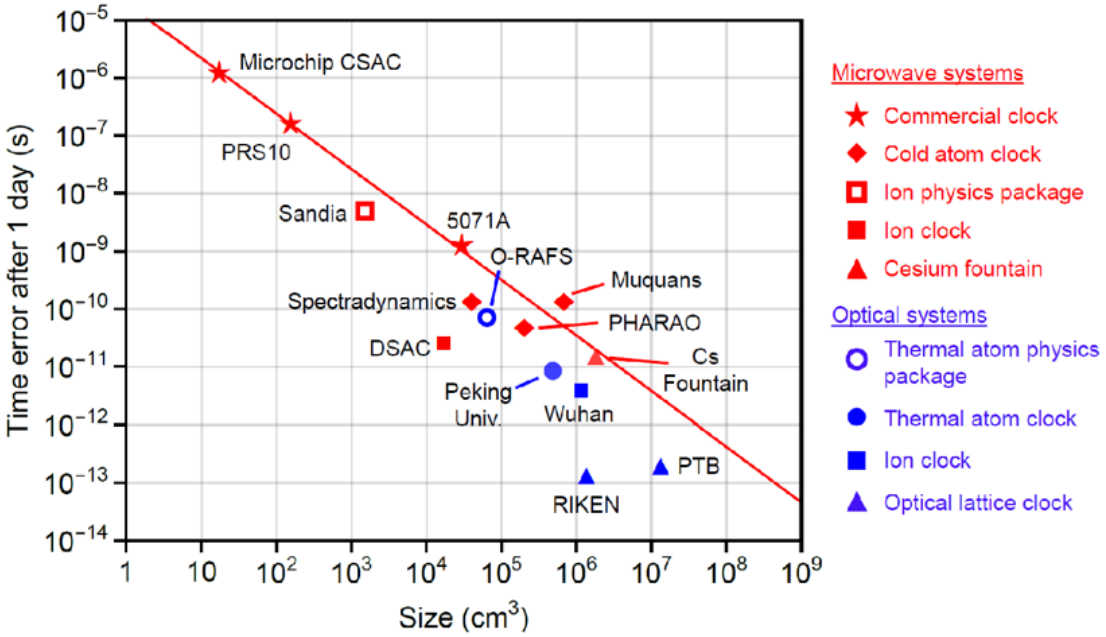

Figure 1.2: Size versus performance graph of various atomic frequency standards from [11], divided between microwave and optical references

it was a microwave clock based on coherent population trapping (CPT) performed on a microfabricated vapor cell containing Cs vapors. Since then, significant progress has been made in miniaturizing atomic vapor-cell devices, with a focus on reducing size, weight, and power consumption while maintaining good performance (see **Figure 1.2**). Microfabricated alkali vapor cells, realized via silicon micromachining and glass-silicon anodic bonding, increase the reproducibility of nominally identical pieces with respect to glass-blown centimeter-scale cells, which are bulkier, present a more artigianal fabrication process and make the control of the atom properties more difficult. Microcells enable the wafer-scale production of miniature, low-power atomic devices [12, 13] with precisely controllable properties. Notably, two-photon Rubidium vapor clocks are well matched to microcells: single-color Doppler-free interrogation simplifies the free-space optics and reduces the linewidth $\Delta\nu$, while the S/N ratio can be improved by increasing the number of atoms through

precise control of the vapor pressure via temperature adjustments. Furthermore, Second Harmonic Generation (SHG) from telecom-band lasers reduces system complexity and size, and fluorescence detection offers a straightforward and efficient readout method. Recent compact demonstrations show that microfabricated vapor cells and modern optics can realize high-performance optical references with simple architectures, approaching hydrogen-maser-like behavior at medium to long averaging times [14, 15]. Key process elements in the fabrication of vapor microcells include deep and selective etching of silicon (e.g., ICP-RIE/DRIE), sidewall conditioning, oxide management, and vacuum-tight wafer bonding [16, 17, 18, 19, 20]. Long-term stability is strongly coupled to the evolution of the cell atmosphere; diffusion barriers and coatings (e.g., Al_2O_3) can dramatically reduce helium permeation and improve lifetime performance [21]. Wafer-level loading

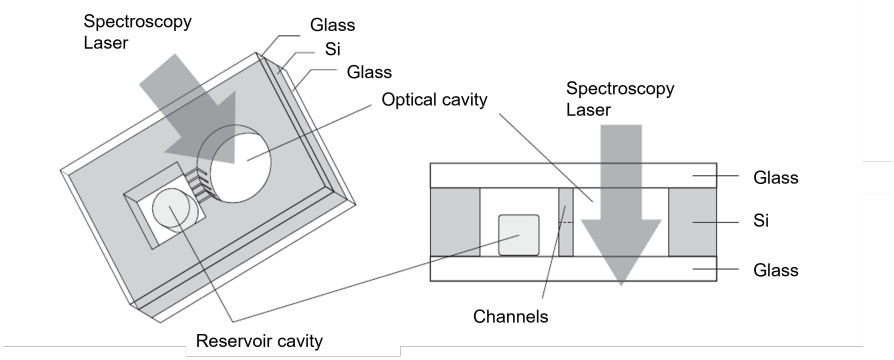

Figure 1.3: Schematic representation of the microfabricated vapor cell structure from [13]. The optical quality where the laser beam passes through is ensured by the glass windows anodically bonded to the silicon frame. The alkali vapor is contained in the main cavity, while the reservoir with the alkali dispenser is connected to the main cavity through narrow microchannels to better control the vapor density and reduce contamination risks. Variations of this design, for example with two isolated cavities and no microchannels when using alkali azides solutions, depend on the filling method used.

strategies further improve cleanliness, repeatability, and device longevity. In fact, over the years, the filling of the microcell with alkali vapors has been carried out using different techniques [22]; considering that alkaline metals react violently with oxygen and atmospheric moisture, this is one of the most complicated and delicate production steps. For macro cells, the usual method was the direct dispensing of a small amount of alkali metal inside the cell before sealing it in a inert environment (such as a glass-blown chamber). In the case of microcells, the most widespread solutions are using alkali azides that decompose to release the alkali vapor when heated or UV activated [13], or *in situ* laser-activated pill dispensers, where a small

pill (microdispenser) containing alkali metal salts is broken by a focused laser beam after the cell is sealed [23]. This post-fabrication method allows for precise control over the amount of alkali vapor released into the cell and minimizes contamination risks during fabrication and sealing, while also allowing for a seal bonding at higher temperatures with respect to alkali azides, thus achieving a better quality seal. While initially a single cavity was used to enclose the pill, liberate the vapors and perform spectroscopy, a further improvement has been to separate the pill reservoir from the main optical cavity through narrow microchannels (**Figure 1.3**), allowing for better control of the vapor density and reducing contamination risks [21].

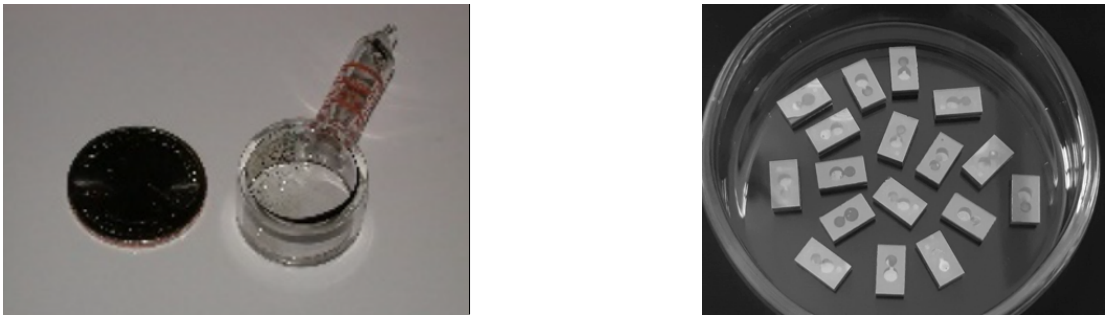

Figure 1.4: Left: traditional glass-blown vapor cell; Right: microfabricated vapor cells. The use of MEMS fabrication techniques allows highly reproducible devices.

1.2 Contributions and thesis roadmap

This thesis advances the microfabrication and spectroscopy of Rb microcells aimed at a compact two-photon optical clock. The work is divided in the following sections:

- **Methodology.** A review of gaussian beam propagation and the ray-transfer formalism is carried out for designing focusing/collimation optics, and the spectroscopic background for Doppler-broadened absorption and Doppler-free two-photon interrogation is developed (**Chapter 2**; cf. [24, 25, 2]).
- **Microfabrication.** A wafer-scale process for the very first *in-house* fabricated silicon microcells is presented, including DRIE of through-wafer cavities, KOH sidewall smoothing, oxide stripping, and anodic bonding to alumina-coated glass; microchannel geometry and permeation mitigation strategies are discussed (**Chapter 3**; cf. [16, 17, 20, 18, 19, 21, 23, 12, 13]).
- **Characterization.** Laser activation and Doppler absorption spectroscopy are performed on the Rb D_2 line to extract atom densities and study filling

dynamics, and a two-photon rack setup at 778 nm with fluorescence detection at 420 nm is built, including power snd temperature stabilization (**Chapter 4**; cf. [15, 14]).

In summary, two-photon Rb vapor-cell clocks combine Doppler-free spectroscopy, fluorescence readout, and telecom-derived laser technology to deliver high-stability optical references in compact form. Microfabricated vapor cells make these systems scalable and manufacturable. The developments presented here provide the fabrication, spectroscopic, and system-level groundwork toward a fieldable Rb optical clock with strong performance at practical SWaP.

Chapter 2

Methodology

This chapter presents the theoretical background and experimental methods used in this work for the characterization of the fabricated microcells and the implementation of a compact atomic clock. It includes a review of the Gaussian beam model of lasers used in the design and manipulation of free-space optics, and the spectroscopic techniques employed in the characterization of the microcells (Doppler spectroscopy) and the clock operation (two-photon spectroscopy). Theoretical spectra of the Doppler broadened Rubidium D_2 line are derived, and the principles of two-photon absorption and its Doppler-free nature are explained.

2.1 Gaussian beam model of lasers

The propagation of a laser beam in free-space, in the fundamental TEM_{00} mode, is described by a Gaussian beam [27], meaning that measuring its intensity along the beam's cross-section one will observe a gaussian profile in space along any transversal direction, almost symmetrically about the propagation axis (z). The normalized intensity of the beam thus follows:

$$I(r,z) = \exp\left(-\frac{2r^2}{w^2(z)}\right) \tag{2.1}$$

where

- $r = \sqrt{x^2+y^2}$ is the distance from the propagation axis z
- $w(z) = w_0\sqrt{1+\left(\frac{z-z_0}{z_R}\right)^2}$ is the beam radius, at which the amplitude of the electric field is reduced by $1/e$ with respect to the peak amplitude along z
- $z_R = \frac{\pi w_0^2}{\lambda}$ is the Rayleigh range, λ the laser wavelength

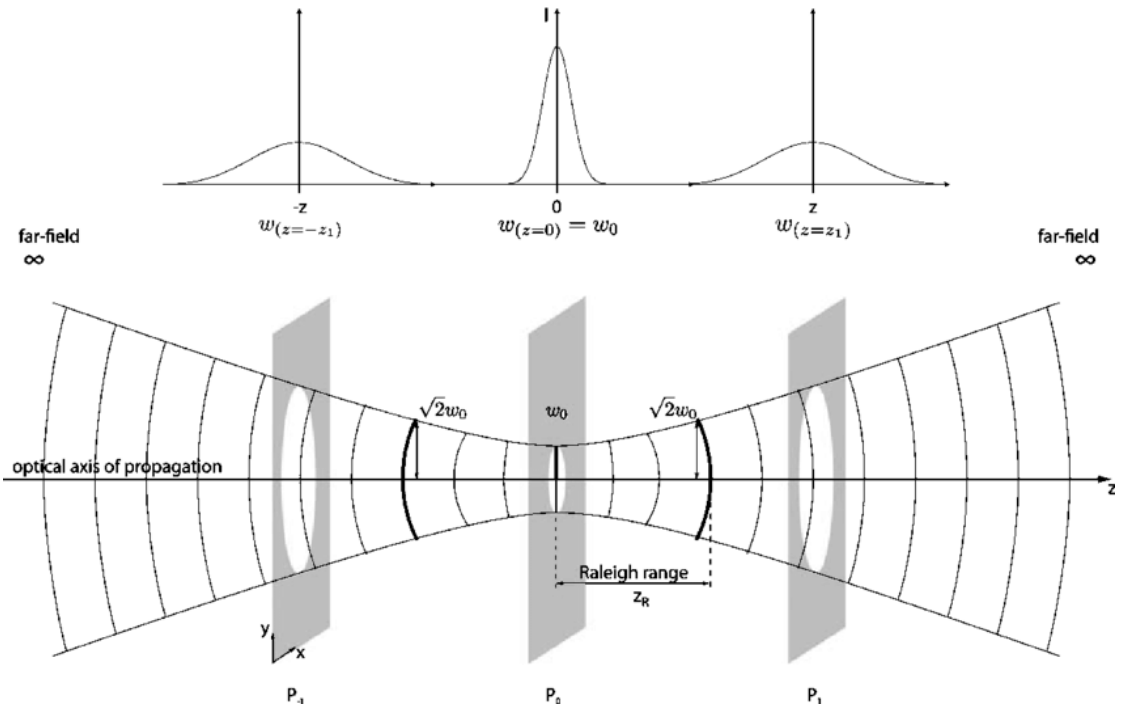

Figure 2.1: Gaussian beam parameters. The beam waist w_0 is located at position z_0 along the propagation axis z. The beam width $w(z)$ increases with distance from the waist, and the Rayleigh range z_R defines the distance from the waist where the beam area doubles. Image from [26].

Some relevant parameters of the Gaussian beam are shown in **Figure 2.1**. The beam waist w_0 is the minimum value of the beam width, located at position z_0 along the propagation axis z, and it defines the spot size of the beam at the focus. The Rayleigh range z_R defines the distance from the waist where the beam area doubles (so where the beam width increases by a factor $\sqrt{2}$). **Figure 2.1** also shows how the wavefronts of the beam curve as the distance from the waist increases, eventually becoming spherical far from the waist. On the other hand, at the waist position, or within the Rayleigh range, the wavefronts can be assumed to be flat, meaning that the beam is collimated in that region, and it closely approximates a plane wave with the wavevector $\vec{k}$ pointing along the propagation direction z. The Rayleigh range, thus, also defines the depth of focus of the beam. The spot size and curvature of a Gaussian beam as a function of z can also be encoded in the complex beam parameter:

$$q(z) = z - z_0 + iz_R$$

This parameter comes useful when studying the propagation of a beam through an optical system of lenses, which can be modeled using the *ray transfer matrix*

method. With this method, any optical system can be represented by a matrix of the kind:

$$M = \begin{bmatrix} A & B \\ C & D \end{bmatrix} = \dots M_3 M_2 M_1 \tag{2.2}$$

which is the product of all the matrices representing the optical components cascaded to form the system, such as lenses, mirrors, and free-space propagations. The entries of such matrices depend on the optical component under exam [28], and for thin lenses are functions of the focal lenght and magnification. Given the complex beam parameter q_{in} at the input of a system, the one at the output can be expressed as:

$$q_{out} = \frac{Aq_{in} + B}{Cq_{in} + D} \tag{2.3}$$

Using these equations it is possible to properly design an optical system so that the output beam has the desired properties in terms of focusing and collimation.

2.2 Spectroscopic techniques

A review of the main theoretical aspects of the spectroscopic techniques employed in this work in both the characterization of the microcells and the implementation of the atomic clock is carried out, with emphasis on their physical origin and the relevant parameters employed in the measurements.

2.2.1 Absorption spectroscopy

Single-photon absorption spectroscopy is a widely used technique to probe the energy levels of atoms and molecules. In transmission mode, it consists in measuring the attenuation of a light beam as it passes through a medium containing the species of interest, while scanning the frequency of the light across the transitions to be studied. When the light frequency is resonant with an allowed transition, photons are absorbed by the atoms, exciting them from a lower energy state to a higher one, and thus causing a decrease in the transmitted light intensity. By recording the transmitted intensity as a function of the light frequency, an absorption spectrum is obtained, which reveals information about the energy levels, transition probabilities, and other properties of the atoms such as the density of vapours and the buffer gas pressure in which they are embedded. In this work, absorption spectroscopy on the D_2 line of Rubidium, shown in **Figure 2.2**, was employed for the characterization of the fabricated microcells.

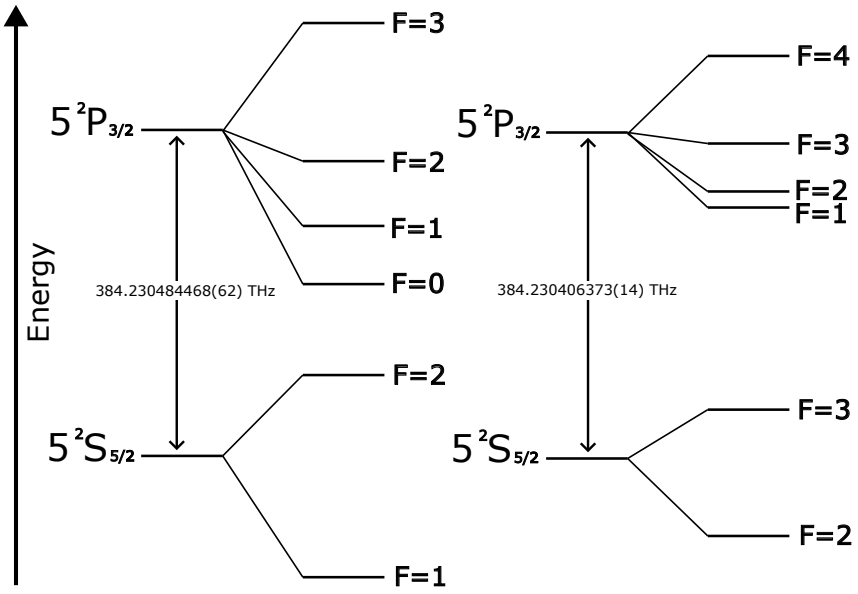

Figure 2.2: Energy level scheme of Rubidium (not in scale), showing the value in frequency of the D_2 line and the hyperfine structure of both ^{87}Rb (left) and ^{85}Rb (right) isotopes.

Atomic absorption

In the linear absorption regime, light intensity in an atomic vapor can be assumed to follow the Beer-Lambert law [29]:

$$I(z) = I_0 e^{-\kappa z}$$

where $I_0 = I(z = 0)$ is the initial intensity. The attenuation coefficient is $\kappa = \sigma n$, with σ being the absorption cross-section (an intrinsic property of the atomic species under examination), and n the atom number density. If light passes through a medium of thickness D containing the atoms, the transmitted intensity $I(D)$ at the output will be:

$$I(D) = I_0 e^{-\kappa D}$$

hence

$$-\kappa D = \ln\left(\frac{I(D)}{I_0}\right) \tag{2.4}$$

Notice that this is a frequency-dependent quantity, since $\sigma(\omega_L)$ depends on the excitation wavelength of the laser. The absorption cross-section $\sigma(\omega_L)$ can be

calculated starting from the atomic structure of Rubidium and its interaction with the laser probe light. Close to resonance with a particular transition, a two level atom model can be used to describe the interaction, where a transition between a ground $|g\rangle$ and an excited $|e\rangle$ state occurs. Assuming low laser power (no saturation), the absorption coefficient can be expressed as:

$$\kappa(\omega_L) = \sigma(\omega_L) \cdot n = \frac{g_2}{g_1} \frac{\pi \omega_{ge} d_{ge}^2 n}{\epsilon_0 \hbar c} g(\omega_L, \omega_{ge}) \tag{2.5}$$

where

- d_{ge}: transition dipole moment
- ω_{ge}: transition angular frequency
- g_1 and g_2: degeneracy of ground and excited states. g_2 together with d_{ge} can be expressed in terms of the line strength $S_{ge} = g_2 d_{ge}^2$
- $g(\omega_L, \omega_{ge})$: lineshape factor

The lineshape factor $g(\omega_L, \omega_{ge})$ describes the broadening of the atomic transition due to various effects. For an ideal transition, with infinitely-lived excited state $|e\rangle$, this would be a delta function centered at the transition frequency. If the transition is only limited by the finite lifetime of the excited state due to spontaneous emission (τ_e), the lineshape is Lorentzian, with a full width at half maximum (FWHM) given by the natural linewidth $\Gamma = 1/\tau_e$:

$$g(\omega_L, \omega_{ge}) = \frac{1}{2\pi} \frac{\Gamma}{(\omega_L - \omega_{ge})^2 + (\Gamma/2)^2}$$

Furthermore, in order to have an absorption peak, atomic transitions must be allowed from the selection rules. For atoms (like Rubidium) having nuclear spin I different from zero, and thus showing a hyperfine structure, transition rules are in terms of the total angular momentum F and require $\Delta F = 0, \pm 1$. Thus, for the D_2 line, in the case of ^{85}Rb:

$$|5^2S_{1/2}\,,\ F_g = 2\rangle \rightarrow |5^2P_{3/2}\,,\ F_e = 1{,}2{,}3\rangle \tag{2.6}$$
$$|5^2S_{1/2}\,,\ F_g = 3\rangle \rightarrow |5^2P_{3/2}\,,\ F_e = 2{,}3{,}4\rangle \tag{2.7}$$

and in the case of ^{87}Rb:

$$|5^2S_{1/2}\,,\ F_g = 1\rangle \rightarrow |5^2P_{3/2}\,,\ F_e = 0{,}1{,}2\rangle \tag{2.8}$$
$$|5^2S_{1/2}\,,\ F_g = 2\rangle \rightarrow |5^2P_{3/2}\,,\ F_e = 1{,}2{,}3\rangle \tag{2.9}$$

Furthermore, for such atoms the degeneracy of the ground state $g_1 = 2(2I + 1)$ can be expressed in terms of the nuclear spin I.

Doppler broadening

In a thermal vapor, the atoms are moving with a distribution of velocities $\vec{v}$ given by the Maxwell-Boltzmann distribution

$$f(\vec{v})d^3\vec{v} = \left(\frac{M}{2\pi k_B T}\right)^{3/2} e^{-\frac{Mv^2}{2k_B T}} d^3\vec{v}$$

where M is the atomic mass, k_B the Boltzmann constant, T the absolute temperature and $v = |\vec{v}|$ the atoms' speed. This motion causes a Doppler shift in the frequency of the light as seen by the atoms, since in the rest frame of each atom

$$\omega'_L = \omega_L - \vec{k} \cdot \vec{v} \tag{2.10}$$

where $\vec{k}$ is the laser wavevector of magnitude ω_L/c in the lab frame, $\vec{v}$ the velocity of the atom in the lab frame, and ω_L and ω'_L are the laser frequencies respectively in the lab and in the atom's reference frames. For each transition $|g\rangle \to |e\rangle$, the absorption lineshape is then obtained by averaging the single atom profile $\kappa_{ge}(\omega'_L)$ over the velocity distribution:

$$\kappa_{ge}(\omega_L) = \int f(\vec{v})\kappa_{ge}(\omega_L - \vec{k} \cdot \vec{v})d^3\vec{v} \tag{2.11}$$

so that, assuming the Lorentzian linewidth is negligible compared to the Doppler width, the resulting lineshape is Gaussian, meaning:

$$\kappa_{ge}(\omega_L) = n \cdot \frac{\pi\omega_{ge}}{\epsilon_0\hbar c}\frac{S_{ge}}{2(2I+1)} g_D(\omega_L, \omega_{ge}) \tag{2.12}$$

with

$$g_D(\omega_L, \omega_{ge}) = \frac{1}{\sqrt{2\pi}\sigma_D} e^{-\frac{(\omega_L - \omega_{ge})^2}{2\sigma_D^2}} \tag{2.13}$$

where the Doppler width σ_D is given by

$$\sigma_D = \omega_{ge}\sqrt{\frac{k_B T}{Mc^2}}$$

The total spectrum $\kappa(\omega_L)$ will be the superposition of all the contributions of this kind for all transitions, each with its transition frequency ω_{ge} and weighted by its line strength S_{ge}. Notice that

$$S_{ge} = g_2 d_{ge}^2 = c_F^2 \left|\langle L_g || \, e\vec{r} \, || L_e\rangle\right|^2 = c_F^2 \frac{9\pi\epsilon_0\hbar c^3\Gamma}{\omega_{ge}^3}$$

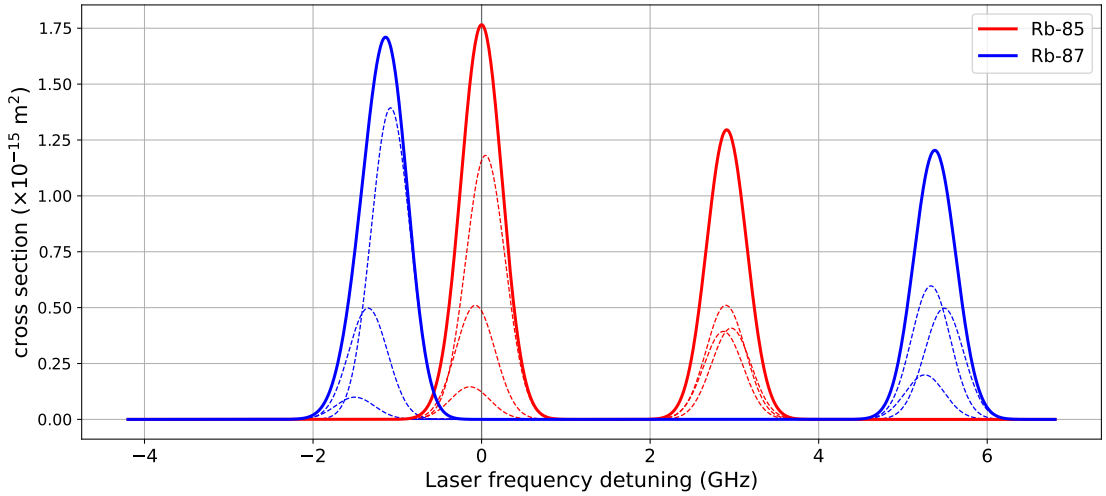

Figure 2.3: Theoretical absorption cross-section of ^{85}Rb and ^{87}Rb. The zero was set at the center of mass of the $F = 3$ triplet of ^{85}Rb transitions.

and the values of Γ, c_F^2 and ω_{ge} for all the transitions of interest in ^{85}Rb and ^{87}Rb can be found in [30, 31, 32, 33, 34, 35]. Also notice that, due to Doppler broadening, the hyperfine transitions from a same ground state to different excited states in the D_2 line (**Equation 2.6**, **2.7** and **2.8**, **2.9**) are not resolved, and the spectrum will consist of only two broad peaks for each isotope, corresponding to the two hyperfine ground states, whose peaks are at the 'center of mass' frequency of each triplet of transitions. **Figure 2.3** shows the theoretical absorption cross-section of both ^{85}Rb and ^{87}Rb, calculated by summing all the transitions obtained from **Equation 2.12** at each frequency.

2.2.2 Two-photon spectroscopy

Predicted theoretically [36] and first observed in the optical range on Caesium [37], two-photon absorption is a second order process that consists in the *simultaneous* absorption of two photons to excite an atomic transition (so a single-step process, as opposed to two-step processes involving an intermediate level[1]) that was shown to be able to cancel Doppler broadening at first order and improve the resolution of spectroscopic measurements by properly acting on the geometry of the light beams in the spectroscopic setup [38, 24]. As previously described, Doppler broadening is

[1]In order to enforce this condition, it is necessary that each of the two photons is off-resonance from any intermediate level, so that only the two-photon transition is excited rather than two consecutive single-photon ones.

due to the thermal velocities of the atoms in a vapour, and in the optical range it can be as high as one hundred to one thousand times the natural linewidth of a spectroscopic line. Each velocity class experiences a different frequency shift. Referring to **Equation 2.10**, the sign of the shift depends on the direction of the photon wave-vector with respect to the atom's velocity. In the lab frame, if two counter-propagating photons having the same frequency ω_L and wavevectors $\vec{k}_1 = \vec{k}$ and $\vec{k}_2 = -\vec{k}$ are absorbed together to excite a transition $|g\rangle \rightarrow |e\rangle$ of energy $\hbar\omega_{ge}$, then conservation of energy will imply (in the atom's rest frame):

$$\hbar\omega_{ge} = \hbar\omega_1' + \hbar\omega_2' = \hbar(\omega_L - \vec{k}_1 \cdot \vec{v}) + \hbar(\omega_L - \vec{k}_2 \cdot \vec{v}) \tag{2.14}$$

$$= \hbar(\omega_L - \vec{k} \cdot \vec{v}) + \hbar(\omega_L + \vec{k} \cdot \vec{v}) = 2\hbar\omega_L \tag{2.15}$$

The terms depending on the atom's velocity cancel out, and all velocity classes contribute to the resonance at the same frequencies, thus eliminating Doppler broadening at first order. When a single monochromatic source is used, a second counterpropagating photon can be obtained by retroreflecting the beam and thus creating a standing wave. The obtained lineshape, in absence of other broadening mechanisms, is then Lorentzian, and only limited by the natural linewidth of the transition. At second order, however, if the light-beam does not fulfill **Equation2.15** but is close to such resonance, two photons coming from the *same* direction can be absorbed together and excite the same transition, if they satisfy

$$\hbar\omega_{ge} = 2\hbar(\omega_L \pm \vec{k} \cdot \vec{v}) = 2\hbar\omega_L \pm 2\hbar\vec{k} \cdot \vec{v}$$

that is to say, if Doppler shift provides the energy defect to reach the resonance. This will create a Doppler-broadened background on top of the Doppler-free peak, whose intensity will however be much lower than the Lorentzian one, since only a single velocity class contributes to it. The overall lineshape will then be a superposition of a narrow Lorentzian peak on top of a broad Gaussian background called *pedestal* [25] (see **Figure 2.4**). Being two-photon absorption a second order process, its excitation probability scales quadratically with the light intensity I, and is much lower than for single-photon absorption: higher light intensity is necessary, thus the use of laser sources is essential. The spectroscopic signal intensity depends both on the excitation probability and on the number of atoms interacting with the light. At a fixed laser power, the latter scales linearly with the interaction area S (the light beam's cross-section), while the former scales as $1/S^2$: proper beam focusing is thus necessary, and reducing the beam waist greatly increases the signal even if fewer atoms are excited (at least up until transit-time broadening becomes an issue [25]). In this work, the transition of interest for clock operation is

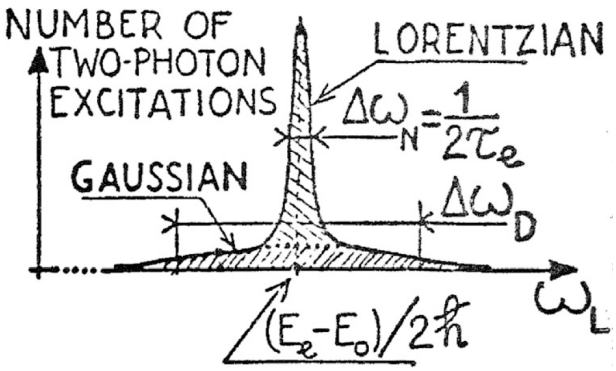

Figure 2.4: Theoretical lineshape of a two-photon transition showing the Doppler-free Lorentzian peak on top of the Doppler-broadened Gaussian pedestal. Historical drawing from [39].

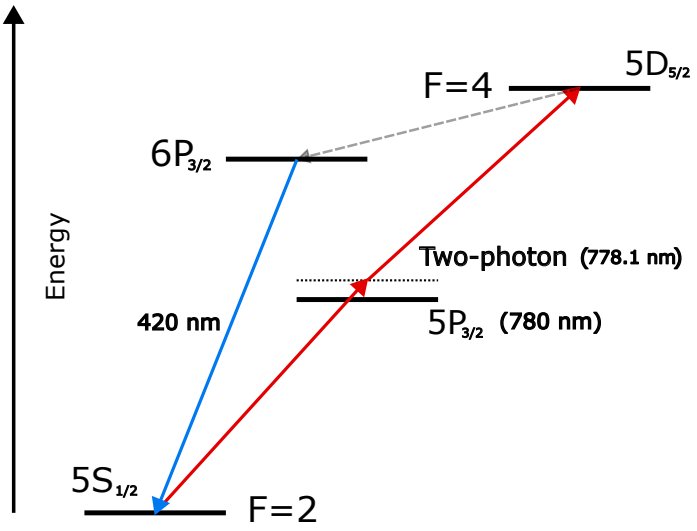

Figure 2.5: Energy level scheme of the two-photon transition in ^{87}Rb from the hyperfine ground state $5^2S_{1/2}\,F = 2$ to the excited state $5^2D_{5/2}\,F = 4$ via the virtual intermediate level. The decay path through the $6^2P_{3/2}$ state is also shown, with the emission of a 420 nm photon[2].

[2]Notice that in this case the spectroscopic signal does not consist in the intensity of transmitted probe light upon absorption, as in the case of absorption spectroscopy, but rather in the intensity of the *fluorescence*, that is the light *emitted* from the alkali atoms relaxing to ground state after excitation.

$$|5^2S_{1/2}\,,\ F=2\rangle \rightarrow |5^2D_{5/2}\,,\ F=4\rangle$$

from the ^{87}Rb isotope, having a frequency of about 385.284566 THz [35] and natural linewidth $\Gamma = 660$ kHz [40]. The transition is probed via a two-photon excitation at 778.1 nm, and the readout is a fluorescence signal resulting from the relaxation of the atoms through a partially non-radiative decay path, which terminates with the emission of a 420 nm blue photon. The energy levels for these transitions are shown in **Figure 2.5**. While in this work the excitation scheme relies on two same-color photons generated from the same laser source, other schemes employing two different colors are also being explored in literature [41], and different readout signals coming from other decay paths can be used [42].

2.2.3 Line broadening mechanisms

Doppler-free two-photon spectroscopy allows to reach very high resolution in the measurement of atomic transitions, giving the possibility to uncover further broadening mechanisms that would be otherwise hidden by Doppler broadening in single-photon absorption spectroscopy. Such broadening mechanisms can be classified into two main categories: homogeneous and inhomogeneous broadening [43]. Homogeneous broadening affects all atoms equally, contributing to the Lorentzian linewidth Γ, and arises from processes such as natural linewidth (ultimate physical limit to the linewidth, caused by the finite lifetime of excited states) and collisional broadening (due to interactions between atoms). Inhomogeneous broadening, on the other hand, arises from variations in the local environment of the atoms (such as their velocity), and contributes to the Gaussian linewidth 2σ, with σ being the standard deviation of the distribution. To this category belong *Doppler broadening* (due to the thermal motion of atoms), variations in local fields (*Zeeman effect*), *transit time broadening* (too short interaction time of the atoms with the light beam) and further Doppler broadening due to misalignment of the counter-propagating beams. In order to separate the contributions of homogeneous and inhomogeneous type to the overall linewidth, the hypothesis of the Lorentzian linewidth being negligible with respect to the Gaussian one, used in **Equation 2.11**, must be lifted, and the obtained profile will actually be a convolution of the two, known as a Voigt profile. Such profile does not have a closed-form mathematical expression, but can be numerically fitted to the experimental data to extract two parameters: a Γ linewidth containing all homogeneous broadening contributions, and a σ parameter accounting for all inhomogeneous contributions. Being two-photon spectroscopy Doppler-free at first order (which is the most prominent inhomogeneous contribution), one can expect that 2σ will be small compared to Γ, so that for practical purposes in this work a first estimate of the overall linewidth will be obtained by fitting a simple Lorentzian profile to the

experimental data, and the Voigt profile will be adopted only in the discussion of the broadening mechanisms in **Section 4.2.2**. A quick overview of the main broadening mechanisms relevant to this work is given below, along with the equations used to estimate their contribution to the overall linewidth in terms of FWHM.

Residual Doppler broadening due to imperfect alignment

When the two photons are no longer exactly counter-propagating their shifts in frequency do not cancel exactly anymore, and the absorption becomes sensitive to the atomic velocity along the bisector of the two beams. Any small angle θ between the incident and reflected beam will thus result in a residual Doppler broadening. In a setting like the one shown in **Figure 2.6** the resulting broadening in terms of

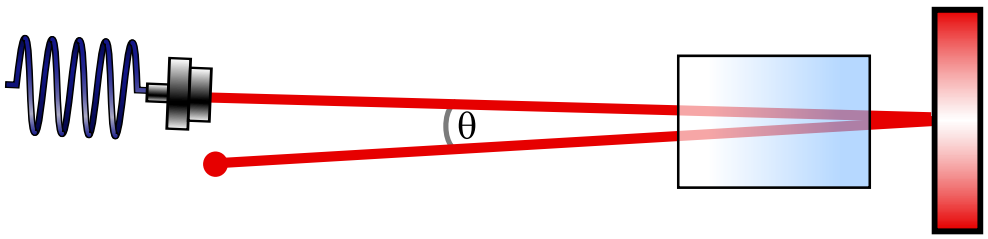

Figure 2.6: Misalignment between incident and reflected beams in a two-photon spectroscopic setup. The angle θ between the two beams causes a residual Doppler broadening.

FWHM can be obtained as [44]:

$$\Delta f_{RD} = \left| \frac{v_p f_0}{c} (1 - \cos\theta) \right| \tag{2.16}$$

where

$$v_p = \sqrt{\frac{2k_B T}{m}}$$

is the most probable velocity of the atoms in a thermal vapor and f_0 is the transition frequency.

Transit time broadening

Transit time broadening arises from the finite time an atom spends in the interaction region with the laser beam. Atoms moving through the beam have a limited interaction time, leading to a quantum uncertainty in their energy levels, and thus a broadening of the spectral lines. The transit time broadening for two-photon

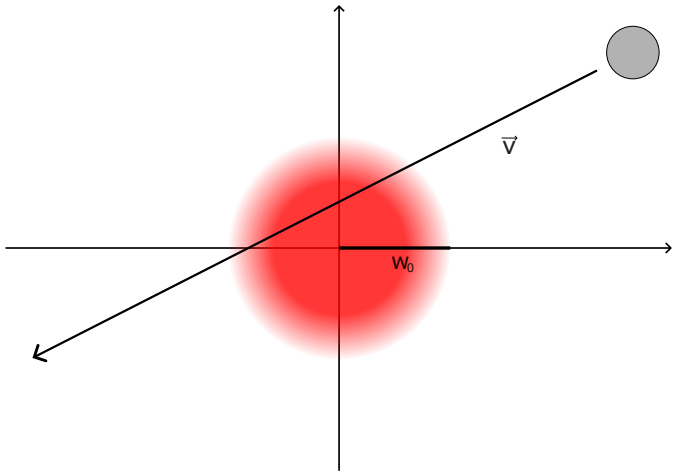

Figure 2.7: Transit time broadening due to the finite interaction time of atoms moving through the laser beam of waist w_0 with velocity v_p.

spectroscopy in a beam with waist radius w_0 (**Figure 2.7**) can be estimated as [45]:

$$\Delta f_{TT} = \frac{\sqrt{\ln 2} v_p}{\pi w_0} \tag{2.17}$$

Zeeman broadening

Zeeman broadening arises from the interaction of atomic magnetic moments with external magnetic fields, leading to a splitting of the hyperfine energy levels into Zeeman sub-levels both for the ground and excited states, and thus a broadening of spectral lines. The excitation of transitions between such levels undergoes transition rules which depend on the polarization of the laser light and the alignment of the beam with respect to the magnetic field. In the experiment presented in this work the natural magnetic fied of the Earth may cause such effects, as no specific magnetic shielding is employed around the physics package. A quantitative evaluation of this effect is not straightforward, but an estimate of its influence will be obtained by comparing the measured Gaussian linewidth with the expected one from other broadening mechanisms.

Homogeneous mechanisms, collisional broadening and cell quality

Lorentzian broadening arises from homogeneous mechanisms that affect all atoms equally. The main contributions in two-photon spectroscopy setups are *natural linewidth* and *collisional broadening*, both acting on the excited state lifetime. Natural linewidth is an intrinsic property of atomic transitions, arising from the

finite lifetime of excited states due to spontaneous emission, and is thus considered the ultimate limit for the spectroscopic line. Its value for a specific transition is tabulated in literature (for instance [40]). Collisional broadening, on the other hand, arises from interactions between atoms and other particles (such as buffer gas atoms and impurities) that perturb the energy levels and shorten the effective lifetime of the excited states [46]. In microcells, collisional broadening can be significant due to the presence of unwanted impurities or buffer gases introduced during the fabrication process, and can be estimated by comparing the measured Lorentzian linewidth with the expected natural linewidth of the transition. Such contributions will be discussed on the two-photon spectra obtained from selected microcells in **Section 4.2.2**.

Chapter 3

Microfabrication

The traditional fabrication methods for alkali vapor cells, such as glassblowing and sealing of macroscopic glass tubes manually filled with alkali metals, are not suited for mass production of compact and reproducible devices. Moreover, their centimeter-scale size prevents their use in miniaturized quantum devices. Microfabrication techniques, borrowed from the semiconductor industry, allow for the creation of miniature vapor cells with precise dimensions and controlled environments, enabling wafer-scale production of batches of nominally identical cells, and eventually the integration with other micro-optical and micro-electronic components [12, 13]. The microfabrication of the alkali vapor microcells is carried out in the *Pi-QuET* cleanroom facilities at the *Istituto Nazionale di Ricerca Metrologica* (*INRiM*) in Turin, following a top-down approach based on photolithography and dry and wet etching techniques. The starting substrate is a 1 mm thick, 4 inch diameter, (100)-oriented, P-type, double-side polished silicon wafer, with a resistivity of 1-10 $\Omega \cdot$ cm. A 2 µm layer of thermal SiO_2 is grown on both sides of the wafer (**Figure 3.2**). The top oxide layer acts as hard mask during the ICP-RIE process, while the bottom one protects the dry-etch instrument chuck form ion bombardment during the etching process. Morover, the SiO_2 layers protect the silicon surfaces maintaining them polished and protecting them from contaminations throughout the fabrication steps, since their area is employed in the anodic bonding process with glass seals. The entire process flow (**Figure 3.1**) described below is optimized for pill-based cells, in which the alkali metal vapor is dispensed upon activation by a high-power laser. The pills are composed by a Zr/Al alloy mixed with a Rb_2MoO_4 salt with a nominal contempt of 0.4 mg of Rb, housed in a small reservoir connected to the main optical cavity through narrow microchannels. This chapter presents the entire microfabrication process, along with the optimization of the process steps, design considerations for the microcell geometry and the strategies adopted to mitigate helium permeation through the microcell walls, which can compromise the long-term stability of the cell atmosphere.

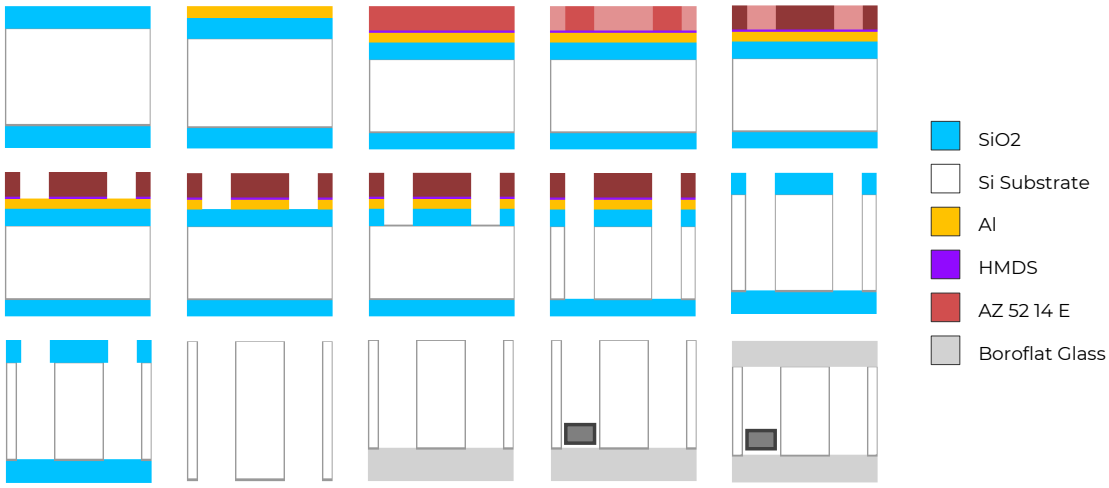

Figure 3.1: Pill-based microcells process overview

Figure 3.2: Initial 1 mm Si + 2 µm SiO_2 wafer

3.1 Aluminium deposition

A thin 200 nm aluminium layer is deposited on one side of the initial wafer (**Figure 3.2**) by electron-beam (e-beam) evaporation (**Figure 3.3**) in the *Temescal FC-200* instrument. The aluminium layer serves as a mask for the ICP-RIE etching of SiO_2 and as additional sacrificial mask for the following Bosch process aimed at creating the passing cavities in silicon. Aluminium is chosen for its good adhesion to SiO_2, its high etch selectivity with respect to the fluorine-based plasma, and its low cost and ease of deposition.

Figure 3.3: Aluminium deposition step

3.2 Photolithography

The patterning of the aluminium layer is performed by standard photolithography techniques, using an image reversal AZ 5214e photoresist (PR) and a NQX4006 Mask Aligner. The photolithography process consists of three main steps: spin coating, exposure, and development. The photomask is fabricated by a commercial provider using high-resolution e-beam writing on a chrome-coated soda-lime glass substrate. The mask contains the negative image of the desired pattern, so that the exposed areas of the photoresist will be removed during development, leaving the unexposed areas to protect the underlying aluminium layer during etching. The mask layout is shown in **Figure 3.4**. Each row consists of 2×2 supercells

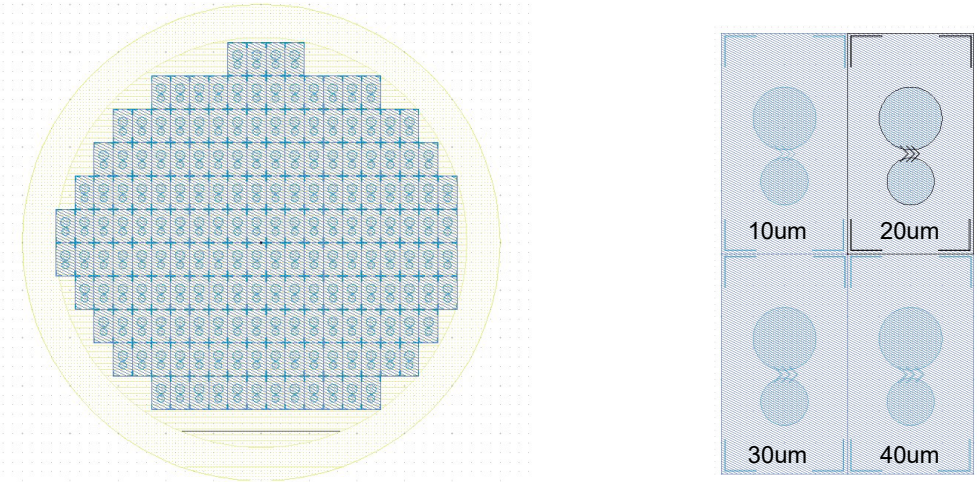

Wafer layout Supercell layout

Figure 3.4: Lithographic pattern design

containing the pattern for 4 microcells with different microchannel widths. Testing

different microchannel geometries allows to study the filling dynamics inside the cells of the Rb vapors upon laser activation of the pill, and to optimize the design for future fabrication runs. The channels form an angle of 45° in order to avoid the possibility of ballistic motion of solid impurities from the pill reservoir to the optical cavity during activation.

3.2.1 Spin Coating

The recipe for the specific PR requires a Pre-Bake step at 120 °C for 5 min, to remove humidity from the wafer surface, then the spinning of a thin (5 Å, almost mono-) layer of HMDS (Hexamethyldisilazane) as adhesion promoter, followed by the spinning of 2 µm (40 s at 1000 rpm speed) of the actual resist. A quick 1 min Soft-Bake at 110 °C is now performed to remove the volatile components of the PR. The procedure is show in **Figure 3.5**

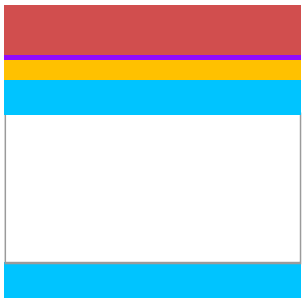

Figure 3.5: Spin coating step

3.2.2 Exposure

The exposure is performed with the NQX4006 Mask Aligner, with a dose of 20mJ/cm^2 for 1 s exposure time, at wavelength of 365 nm (mercury lamp i-line, near-UV). The chromium/quartz mask written through e-beam lithography contains the negative image of the desired pattern. At this point, a Post-Exposure Bake at 120 °C for 2 min is performed as image-reversal step, and a 40 s flood exposure under the UV LED lamp again at 365 nm wavelength completes the crosslinking of the resist, inverting its polarity to obtain the desired pattern. The process is depicted in **Figure 3.6**.

3.2.3 Development

The soluble part of the PR is removed in a AZ400K 4:1 developer aqueous solution containing buffered potassium, at 20 °C temperature for about 1 min (**Figure 3.7**).

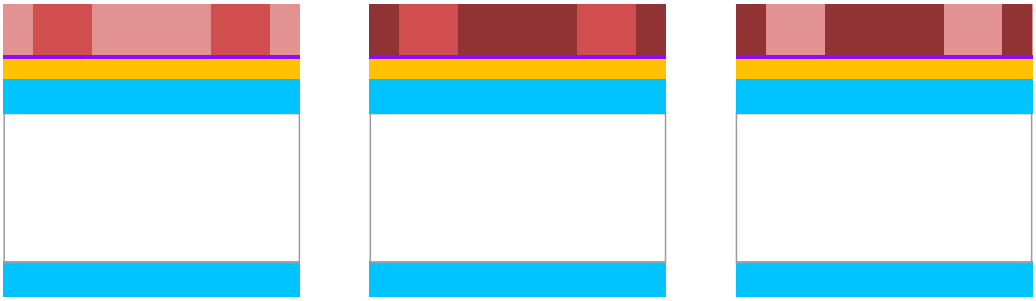

Mask Align Exposure Post-Exposure Bake Flood Exposure

Figure 3.6: Exposure and image reversal step

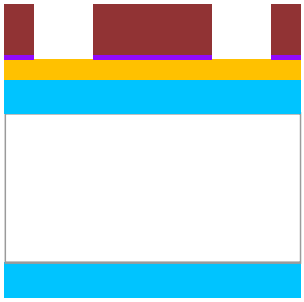

Figure 3.7: Development step

3.3 Aluminium etching

The Al etch is performed using the TechniEtch Al80, a commercial tri-phase solution of H_3PO_4, CH_3COOH and HNO_3 which completely dissolves the 200 nm of Al in about 4.5 min (**Figure 3.8**).

3.4 SiO_2 ICP-RIE

The thin 2 µm SiO_2 layer is etched by a dry etching process in an Inductively Coupled Plasma - Reactive Ion Etching (ICP-RIE) system, the *Oxford Instruments PlasmaPro 100 Cobra*, using a CHF_3/C_4F_8 gas mixture, with gas flow rates of 30/40 sccm. The ICP-RIE technique combines the high plasma density of an ICP source with the directionality of a RIE source, allowing for high etch rates (up to

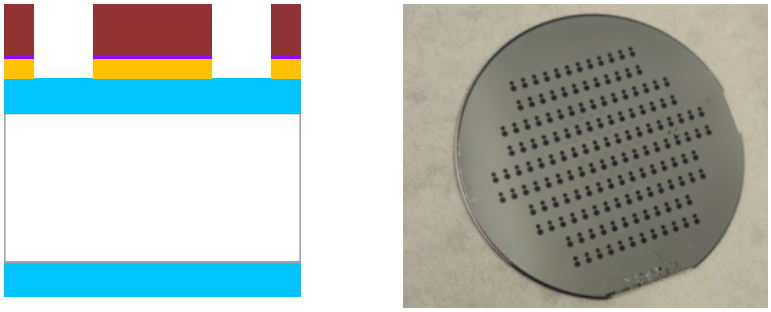

Figure 3.8: Patterned aluminium mask

10 times higher than conventional RIE) while maintaining good anisotropy and low damage to the substrate.

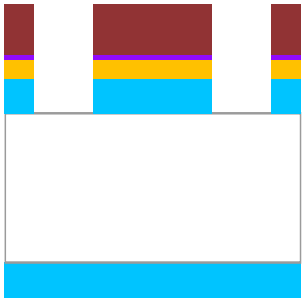

Figure 3.9: SiO_2 etching step

Chamber heater	40 °C
Table chiller	5 °C
Table RF	75 W
ICP Power	2000 W
APC	7 mTorr
CHF_3 gas flow	30 sccm
C_4F_8 gas flow	40 sccm

Table 3.1: ICP-RIE etch of 2 µm SiO_2 process parameters

The recipe (**Table 3.1**) is optimized to achieve high selectivity for SiO_2 over Al, so that the aluminium mask can withstand the entire etching process without being completely removed and to be employed as additional sacrificial mask in the following Bosch process. The etch rate is 160 nm/min, so that the whole process

takes about 13 min. The result (**Figure 3.9**) is a clean and well-defined pattern in the SiO_2 layer, which will serve as a hard mask for the subsequent silicon etching step.

3.5 Si DRIE (Bosch process)

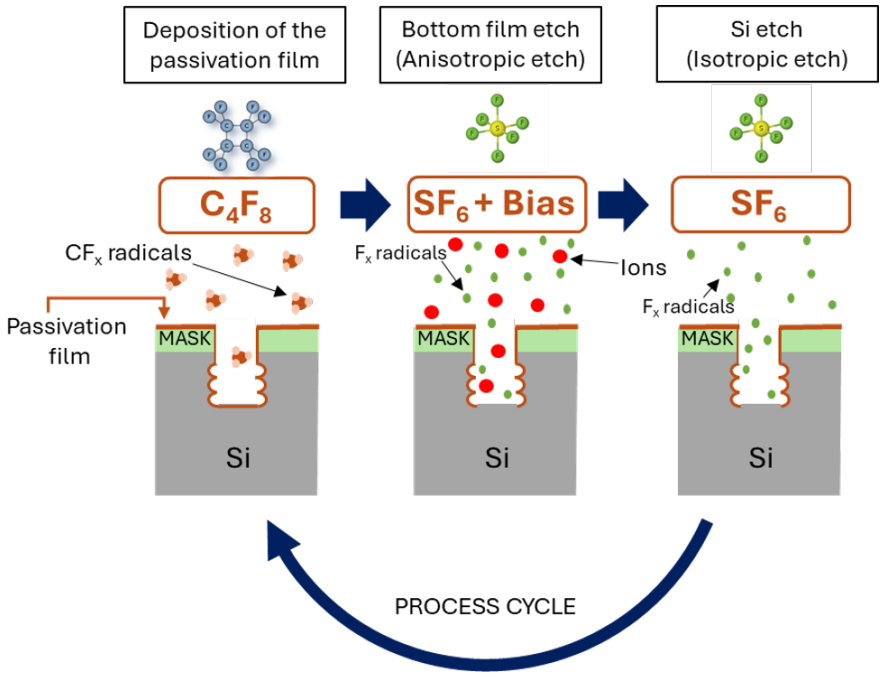

Figure 3.10: Graphical representation of a complete Bosch cycle

The creation of the passing cavities in a 1 mm Si wafer was performed using the Bosch process, based on the Deep Reactive Ion Etching technique and patented in 1996 by Laermer in the context of MEMS microfabrication [16] (Bosch is indeed one of the most recognized companies in this industry). It is a highly anisotropic dry-etching method, able to dig deep trenches with an aspect ratio up to 30:1 in the vertical direction, now commonly employed also in the fabrication of through-silicon vias for 3D integrated circuits [17]. The process consists in the repetition of three main steps (**Figure 3.10**): a passivation (deposition) step, based on C_4F_8, a break step based on ion bombardment, and a plasma etching step, based on SF_6 plasma. In the first step, the C_4F_8 plasma deposits a thin ($\approx$ 50 nm) Teflonlike polymer protective layer isotropically on all surfaces. In the second step, the vertical surfaces are exposed to ion bombardment from the plasma, which gives the directionality to remove the polymer layer from the bottom of the trench, while leaving it intact on

the sidewalls. In the third step, the SF_6 plasma creates a mixture of reactive ions and radicals which attack the exposed silicon surface in both vertical and lateral directions, creating a rough and isotropic etch profile. However, surfaces protected by the polymer remain intact. By alternating these steps with the appropriate time ratios and gas flow rates, deep trenches with nearly vertical (90° ± 2°) sidewalls can be achieved. While trenches up to 500 µm are an established technology, the use for through-wafer etching up to 1 mm is more recent, and requires a careful optimization of the process parameters to avoid problems such as notching, bowing, and sidewall roughness (scalloping). The millimeter deep trench also leaves a so called *grass* at the bottom of the wafer, made up of Si pillars that cause the so called *Black Silicon* phenomenon. The two latter problems, in particular, may cause contaminants or the atomic vapor itself to get trapped in the roughness features, and thus it is important to minimize them as much as possible.

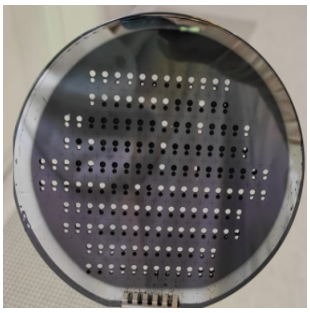

Before optimization

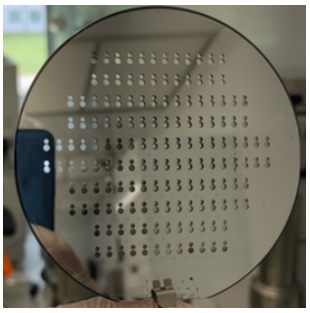

After optimization

	Deposition	Break	Etch
Time	1.7 s	1.9 s	6.0 s
Pressure	35 mTorr	25 mTorr	50 mTorr
Table RF	Off	50 W	Off
ICP RF	2500 W	2000 W	2500 W
C_4F_8 flow	150 sccm	10 sccm	-
SF_6 flow	10 sccm	200 sccm	200 sccm

Table 3.2: ICP-DRIE etch of 1mm Si - Bosch process optimized parameters. The Table Chiller was set at 5°C, and the total number of cycles is 710.

We optimized the recipe on an *Oxford Instruments PlasmaPro 100 Cobra ICP-RIE* system, for a total of 710 cycles, each with a deposition time of 1.7 s, a break

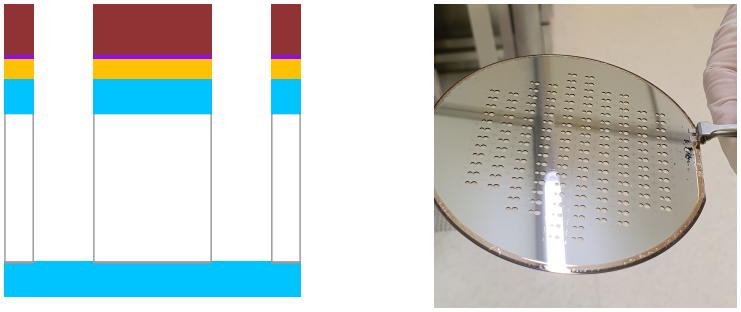

Figure 3.11: Si through-wafer DRIE etching step

time of 1.9 s and an etch time of 6 s, with C_4F_8/SF_6 gas flow rates of 150/200 sccm (**Table 3.2**). With an etch rate of about 1 µm/min, the whole process amounts to 2 h, and is tuned to completely remove silicon from the cavities and leave a thin SiO_2 layer at the bottom, which acts as etch-stop (the Bosch process is selective for Si with respect to SiO_2) and protects the chuck of the instrument from damage, as shown in **Figure 3.11**.

3.6 Piranha cleaning

Fluorocarbon polymers and other organic residues from the previous steps, such as photoresist, are removed by an acetone bath, followed by an isopropanol rinse and a piranha cleaning step (a mixture of sulfuric acid and hydrogen peroxide, H_2SO_4:H_2O_2 in 3:1 ratio). The piranha solution is a strong oxidizer, which effectively removes organic residues without attacking Si or SiO_2, leaving the surface hydrophilic and ready for the next step. It also dissolves any remaining aluminium, so it is important to perform this step only after the aluminium mask is no longer needed (**Figure 3.12**).

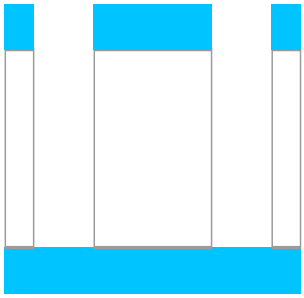

Figure 3.12: Piranha cleaning step

3.7 KOH wall polishing

The Bosch process leaves typical morphological features called scallops, as appreciable in **Figure 3.13**. These structures could create favored condensation sites for the atomic vapors, potentially reducing the Rb concentration and the microcell life-time.

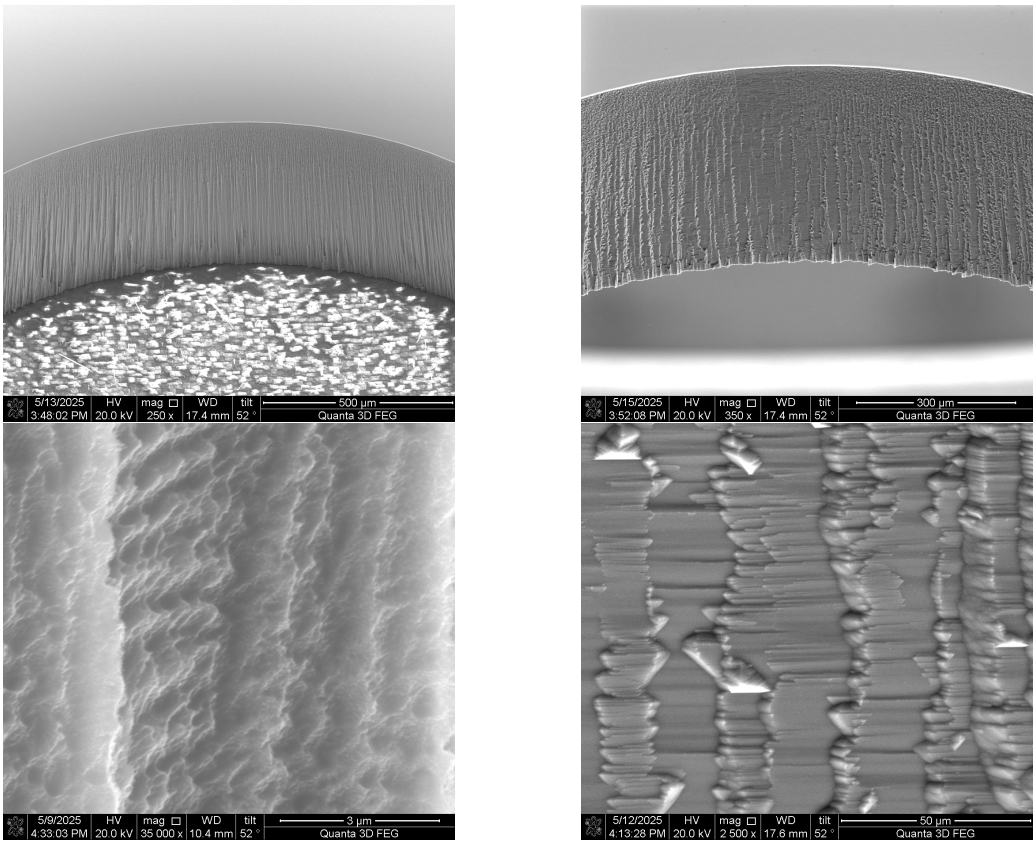

Pre-KOH treatment Post-KOH treatment

Figure 3.13: SEM images of the optical cavity before and after KOH polishing

To mitigate these effects, a wet etching (polishing) step in a heated KOH solution (45% wt in H_2O) for 25 min was performed, so that preferential crystallographic planes emerge on the surfaces, which however present lower roughness than the untreated sidewalls (**Figure 3.13**). KOH, indeed, is a highly anisotropic etchant for Si, and etches the (100) plane about 600 times faster than the (111) plane. Such process (process step in **Figure 3.14**) may also provoke an unwanted enlargement of the microchannels' width, so that it ultimately further deviates from its nominal

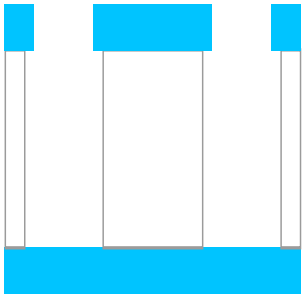

Figure 3.14: KOH wall polishing step

value defined during the design of the layout. A study of such effect is reported in the next subsection.

3.7.1 Microchannels enlargement study

The deviation of the microchannels' width from their layout nominal value was analyzed in a process study, for a KOH polishing carried out at different temperatures, keeping the etching time at 25 min. The expected behaviour is exponential

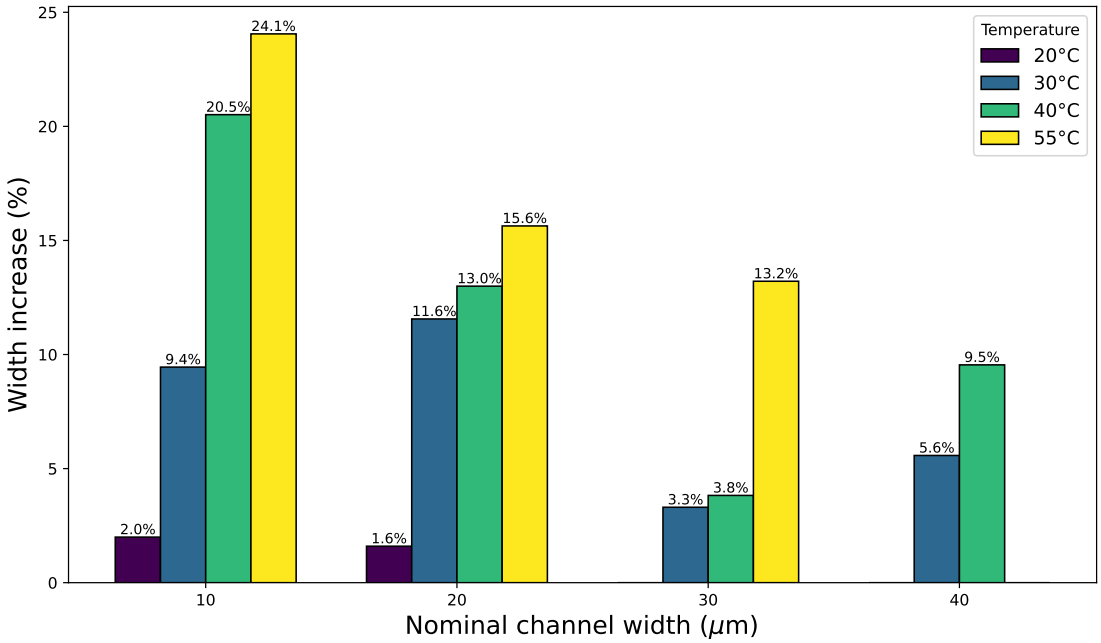

Figure 3.15: Microchannels relative width increase for different KOH polishing temperatures

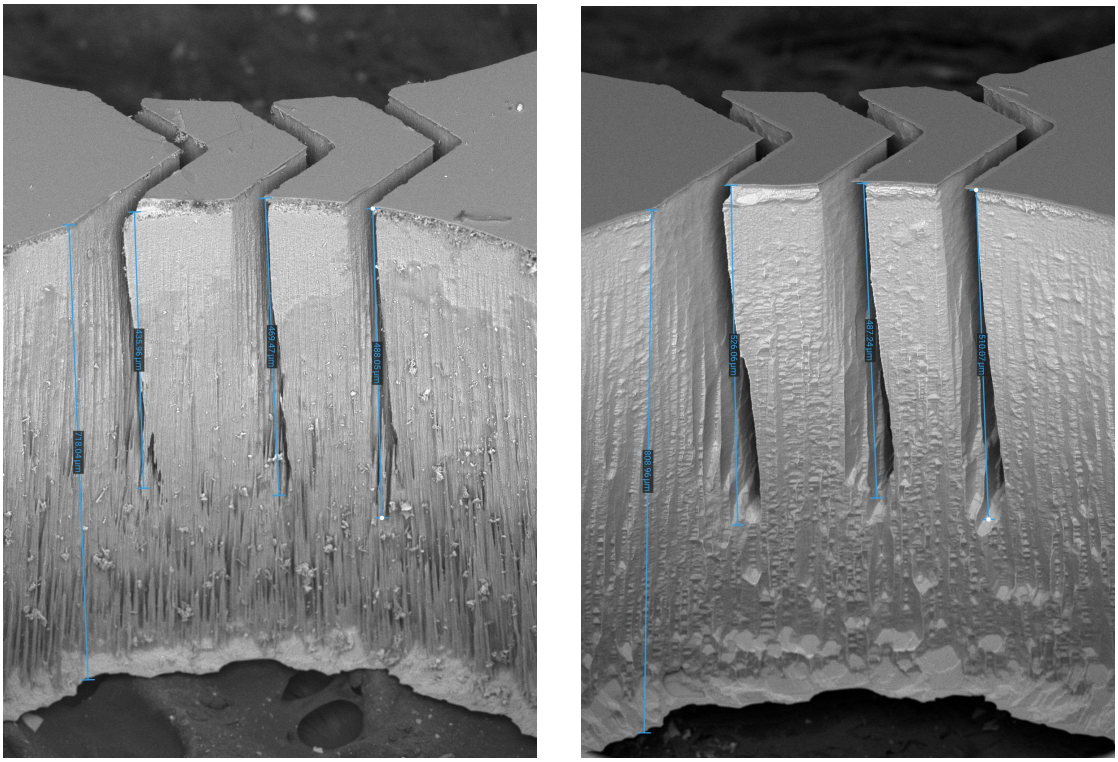

Pre-KOH treatment Post-KOH treatment

Figure 3.16: SEM images of the 20 µm microchannels before and after KOH polishing at 55 °C

with respect to temperature [47]. The results are summarized in **Figure 3.15**, showing an increase of the width up to 24% for a polishing temperature of 55 °C. An example of how the microchannels change upon KOH polishing is shown in **Figure 3.16**. The optimal trade-off between sidewall roughness removal and microchannel enlargement was found at a temperature of 55 °C, as suggested in [20], which was thus chosen for the fabrication of the microcells.

3.8 SiO_2 removal

The oxide layer stripping is performed through HF wet etching chemistry [48]. The use of such chemical leaves monochrystalline silicon completely untouched (**Figure 3.17**), and reveals the pristine high-quality polished silicon surfaces required to perform anodic bonding.

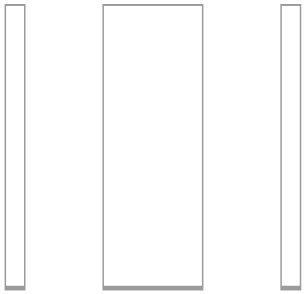

Figure 3.17: SiO_2 removal step

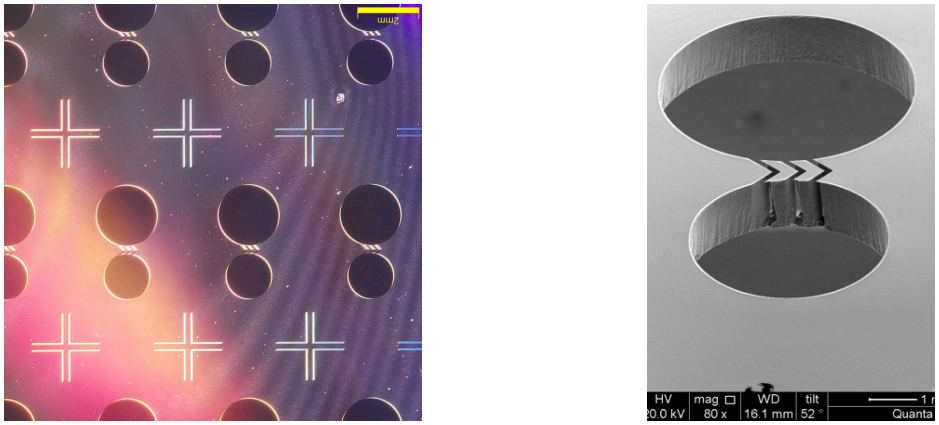

Figure 3.18: Patterned silicon wafer with microcell geometry

3.9 Anodic Bonding

The cells batch is completed by enclosing the processed silicon wafer between two 4 inches, 0.5 mm thick, double side polished Boroflat glass layers, previously coated, on the inside face, with a thin 20 nm Al_2O_3 layer (again using the *Temescal FC-200* instrument). Such alumina layers help avoiding the diffusion through glass [49] of outside atmospheric helium inside the cell, which may perturb the spectroscopic signal limiting the excited state lifetime [21]. Anodic bonding is a wafer sealing technique proposed first in 1969 by Wallis and Pomerantz [18], as a lower temperature alternative to glass frit bonding, for both encapsulation and Si-Si wafer bonding through glass intermediate layer. It became an essential step in MEMS microfabrication processes, and is now used also to encapsulate vapor microcells [19]. The bonding mechanism is attributed to mobile ions in the glass. Boroflat glass is chosen specifically for its content of sodium ions, and also for its thermal expansion coefficient similar to that of silicon, so that no mechanical stress is introduced upon bonding [50]. It is also conveniently transparent at the

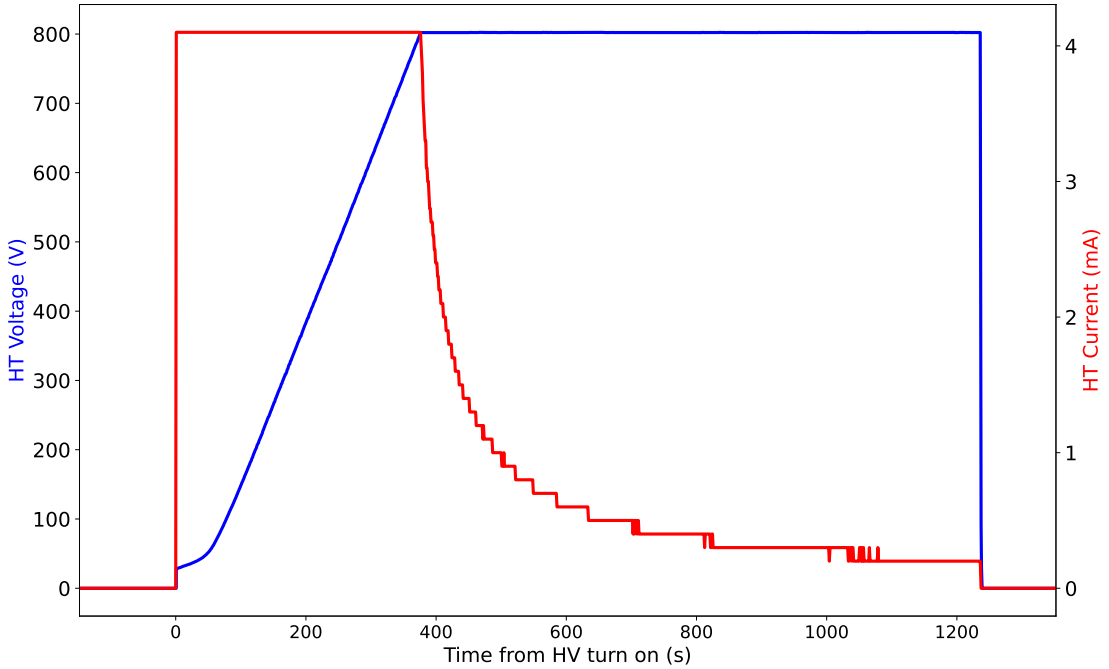

Figure 3.19: Current and voltage behavior during anodic bonding process. The ionic current allows real-time monitoring of the reaction.

wavelengths of interest for the Rb optical clock. At an elevated temperature of 350 °C (still below the glass softening point), the positive ions such as Na^+ have an increased mobility (the glass starts behaving as an electrolyte [51]) and, thanks to a high applied voltage of 800 V, are attracted to the negative electrode on the glass surface and are removed. The negative O_2^- ions left in the glass form a space charge layer of few microns adjacent to the silicon surface, on the glass side. The large applied potential drops on this small depleted region, resulting in a large electric field that pulls the two sides into contact, and starts a chemical reaction that leads to the formation of strong Si-O bonds. This is thus an irreversible process, which creates a hermetic seal between silicon and glass. As more ions are removed, the depleted region will increase in width, causing the electric field to decrease, and the current (which is exponential in the field) to eventually die out once the process is completed (**Figure 3.19**). The instrument used is an *AML Aligner Wafer Bonder*. The cathode consists of a graphite plate, that allows for a uniform application of the high voltage on the glass surface, while the anode is a needle contacting the silicon wafer from the side. The application of a force between the two plates helps increasing the contact surface and favours a more uniform reaction. After the preform bonding with the first glass layer, the commercial pills from *SAES Getters* are manually dispensed inside the reservoir cavities, with the wafer on a hot

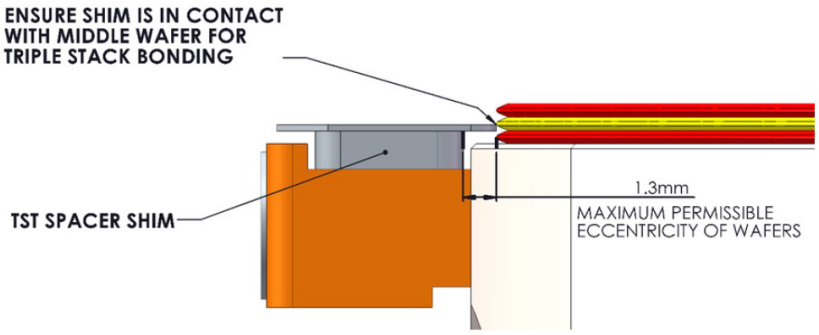

Figure 3.20: Triple-stack configuration for seal bonding

plate at 80°C to limit moisture absorption by the pills. The seal bonding is then performed, enclosing the pills in high vacuum ($\approx 1 \times 10^{-5}$ mbar) and completing the cell structure. Since in both steps it is required that the anode only contacts silicon, while the cathode only contacts the glass, a triple-stack configuration is used during the seal bonding to bypass the underlying glass (**Figure 3.20**).

Plates temperature	350 °C
Applied force	700 N
Applied Voltage	800 V
Current limit	8 mA
Final current	0.4 mA
Total passing charge	2043 mC

Table 3.3: Preform bonding process parameters

Each bonding takes about 20 mins of net process time, from the application of the voltage to the current extinction, which are however preceded by a heating ramp of about 30 mins to reach the process temperature, and followed by a cooling ramp of similar duration to avoid thermal shocks to the bonded wafers, plus the necessary pump and vent times of the bonding chamber to reach the desired vacuum level. The process parameters are summed up in **Table 3.3**. This sequence ensures the integrity of the alkali vapor and the microfabricated structures, preparing the cells for subsequent activation, characterization and use (**Figure 3.21**).

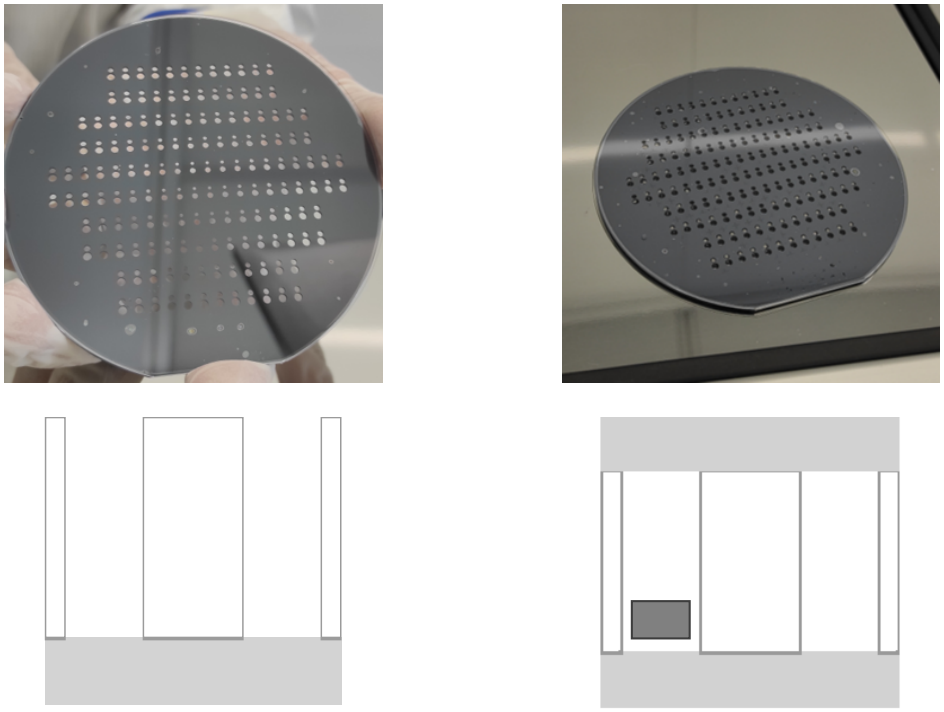

Preform bonding Seal bonding

Figure 3.21: Wafer bonding and filling step

3.9.1 Wafer signing

To facilitate the characterization, handling and classification of the microcells in the subsequent steps, the wafer is signed with a marker by highlighting each row of microcells with a different letter and each 2 × 2 supercell with a different number, as shown in **Figure 3.22**. Each cell is then assigned a number from 1 to 4 (corresponding to channel widths from 40 µm to 10 µm) inside of its supercell, so that each microcell can be uniquely identified by a code such as A3/2 (row A, supercell 3, cell 2).

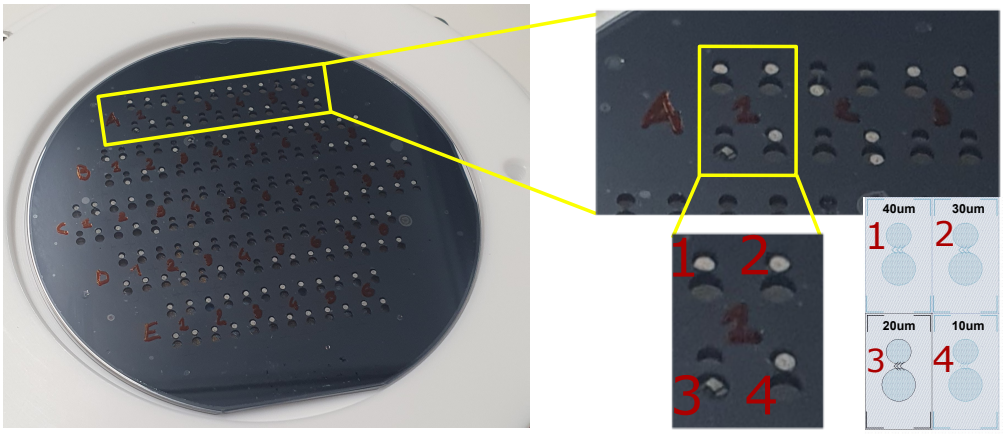

Figure 3.22: Wafer signing step

Chapter 4

Characterization

After processing and sealing the Silicon wafer as described in the previous chapter, we are left with a complete batch of microcells. Such cells need now to be *activated* (i.e. filled with Rubidium vapor by heating up the pill microdispenser in the reservoir cavity) and then characterized in terms of their optical quality and Rubidium content for the application to atomic clocks. The important aspects to be considered in the evaluation of the quality of a microcell are the signal amplitude, proportional to the number of alkali atoms present in the optical cavity, and the level of impurities in the vapor. The signal amplitude quality can be

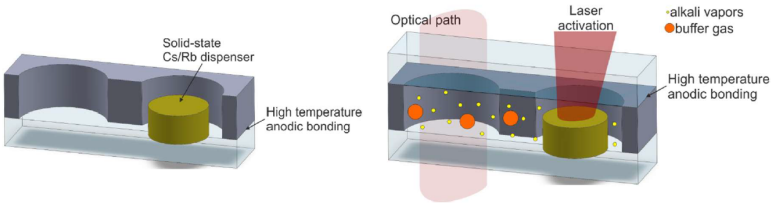

Figure 4.1: Activation of a microcell based on solid-state pill microdispenser by means of a focused high-power laser beam. Figure form [52]

checked by verifying that the Rubidium density inside the cell has reached the condition of saturated vapor pressure at the operating temperature, and can be probed through Doppler spectroscpy. The level of impurities is more difficult to measure directly. An indirect indication of the absence of contaminants is the measurement of the linewidth of a narrow transition, which can be detected using high-resolution two-photon spectroscopy. If the detected transition linewidth exhibits a homogeneous broadening higher than the one due to natural linewidth, one can attribute the excess broadening to residual inert gases present in the cells that introduce collisional broadening (see **Section 2.2.3**). Real-time monitoring of the absorption spectra during the activation process also allow to study the

dynamics of the filling of the cell, and to link it to the diffusion of Rb vapors from the reservoir cavity to the optical cavity through the microchannels. The activation of the microcells through a high-power laser (**Figure 4.1**) and the observation of their Doppler spectra is carried out using a custom automatic absorption spectroscopy setup built in the *PiQuET* labs [53], that allows for simple, wafer-level operation. Following the activation and assessment of vapor filling, the sealed wafer is cut by means of a diamond saw, and the individual cells are obtained. A cell can then be mounted in the rack-scale two-photon spectroscopy setup, where the actual atomic signal useful for clock operation can be observed.

4.1 Cell activation and absorption spectroscopy

Once the wafer is sealed, the microcells in the batch need to be filled with atomic vapors following the dispensing pill activation, and then characterized in terms of their Rubidium content and optical quality. Both tasks were carried out using the custom automatic setup built in *PiQuET* labs [53]. The spectroscopic part of the setup is composed of a tunable diode laser at 780 nm, which is scanned in time over the D_2 line of Rubidium using a triangular wave. A retroreflector is then placed below the wafer, directing light to a $\lambda/4$ polarizer, a beam-splitter, and finally a photodiode used to measure the transmitted intensity. Such laser is aligned to the optical cavity by calibrating the setup (both manually, acting on the mirrors, and by compensating rotation offsets via software), and the obtained frequency scan is compared to a reference *macro* (glass-blown, centimeter-scale) Rubidium cell. The setup allows to perform both absorption spectroscopy (Doppler spectra) and saturated absorption spectroscopy (sub-Doppler spectra [43]), which allows to resolve the hyperfine structure of the atomic transitions and to measure the linewidth of the transitions, but in this work only the former is employed. The activation of the microcells is performed by using a high-power (1.4 W) 1111 nm continuous wave (CW) laser able to heat up the pills contained in the reservoir cavity and liberate the atomic vapor. Such laser is focused on the reservoir cavity of each cell by means of a motorized stage that can move the wafer in the x and y directions with respect to the fixed beam. The activation laser is turned on for 4 s to heat up the pill and release the Rubidium vapor. The system, shown in **Figure 4.2**, then allows for real-time monitoring of the absorption spectra during the activation process through periodic scans of the spectroscopy laser frequency, so that an absorption profile is acquired every few seconds after the activation laser is turned off. By tracking the absorption peaks over time, it is possible to acquire useful information about the dynamics of the process and determine when the Rubidium vapor has reached a stable pressure inside the microcell. The setup is also equipped with an oven (in which the wafer is placed) and a temperature

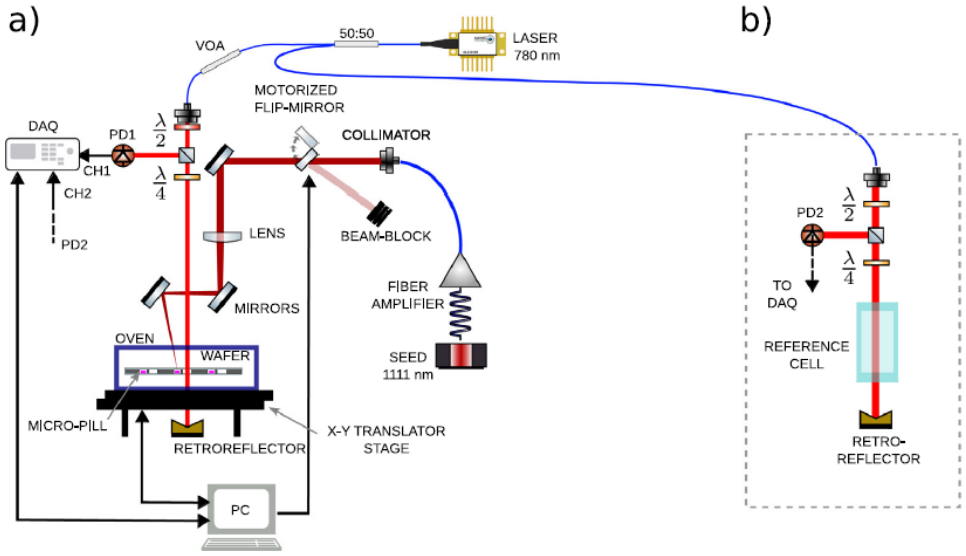

Figure 4.2: Schematic representation of the automatic setup used for the activation and characterization of the microcells. From [53]

controller that heat the microcells to the desired temperature of typically ~ 65 °C and allow to control the vapor pressure of Rubidium inside them. Due to the specific design of the system, the acquired signal requires some post-processing in order to remove unwanted effects that can affect the quality of the spectra. Details on the post-processing of the atomic spectra are provided in **Section 4.1.1**.

4.1.1 Signal post-processing

Two main effects are considered: a linear increase in intensity due to the laser current modulation, and a sinusoidal trend arising from the etalon modulation due to parasitic reflections between parallel surfaces along the optical path. The post-processing of a single scan is hereby presented, along with the extraction of the atomic number density from the processed absorption profile.

Linear trend

The laser frequency is scanned using a current modulation of the probe laser. This causes an unwanted change in the laser output power, due to the linear relationship between injected current and optical power in diode lasers [54]. Such contribution can be removed by fitting the non-absorbing parts of the spectrum (the "flat" parts) to a linear function, and then dividing the whole signal by the fitted line to obtain a normalized spectrum. The residual signal after this procedure, shown in **Figure**

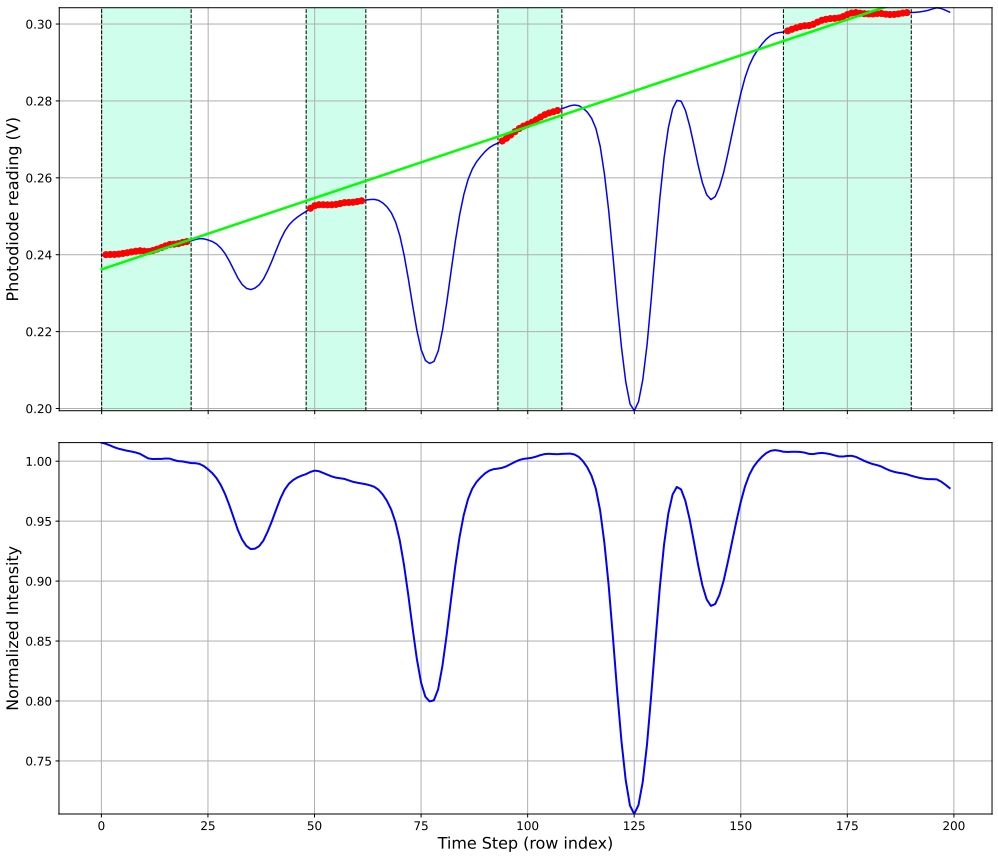

Figure 4.3: Intensity normalization; Top: raw signal with fitted linear trend (green line); Bottom: normalized signal.

4.3, suggests the presence of another sine-like modulation superimposed on the signal, which can be attributed to etalon effects. The analysis is carried on in the following paragraph.

Etalon modulation

In spectroscopy setups, unwanted parallel surfaces (e.g., a detector window) introduce parasitic etalon effects. The true signal $S_0(\lambda)$ is modulated by an oscillatory component due to interference:

$$S(\lambda) = S_0(\lambda) \cdot T(\lambda)$$

A simple model consists in assuming a Fabry-Pérot cavity with two identical, partially reflective, plane-parallel surfaces separated by a distance d, with no absorption losses. The medium between the surfaces has refractive index n (usually

air, $n = 1$), and each surface has reflectivity R, thus transmittivity $T_0 = 1 - R$. The modulated signal will be [55]:

$$S(\lambda) = S_0(\lambda) \left[C + A \cos \left(\frac{4\pi n d \cos \theta}{\lambda} + \phi \right) \right]$$

where A and C are constants depending on the reflectivity R, θ is the incidence angle (usually close to zero), and ϕ a phase term depending on the initial conditions. So, given the signal, one can again fit the theoretically "flat" parts (those where no absorption takes place) to a sinusoidal function, using the amplitude, the frequency, the phase and the constant offset as fitting parameters (see **Appendix A** for the full derivation). Once the fit is done, the etalon modulation can be removed dividing the signal by the fitted function. The intensity signal thus obtained (**Figure 4.4**)

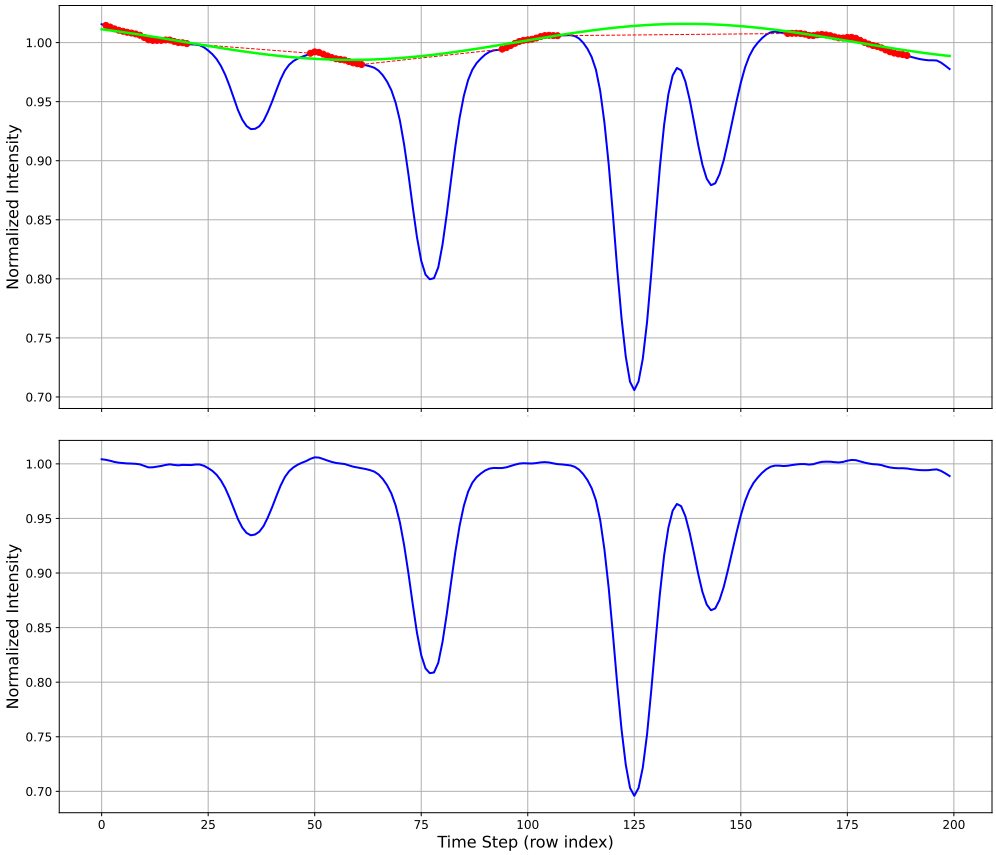

Figure 4.4: Removal of etalon effect; Top: signal with etalon modulation and the fitted sinusoidal function (green); Bottom: detrended.

can be directly linked to the atomic absorption profile using **Equation 2.4** from

Section 2.2.1 and dividing by the optical path length D, which is twice the cell length d since the spectroscopic beam passes through the cell twice after being reflected below the wafer (see **Figure 4.2**).

Atom number density extraction

From the absorption coefficient $\kappa(\omega_L)$ obtained through the Beer-Lambert law (**Equation 2.4**)

$$\kappa = -\frac{1}{D}\ln\left(\frac{I(D)}{I_0}\right)$$

one can extract the atom number density n using **Equation 2.5** from **Section 2.2.1**. In particular, one can fit the theoretical absorption cross-section profile $\sigma(\omega_L)$ (**Figure 2.3**) multiplied by n to the experimental $\kappa(\omega_L)$, using n as fitting parameter. Being the vapor composed of a natural mixture of ^{85}Rb and ^{87}Rb isotopes, the total absorption coefficient will be the weighted sum of the two isotopes' cross-sections:

$$\kappa(\omega_L) = n_{85} \cdot \sigma_{85}(\omega_L) + n_{87} \cdot \sigma_{87}(\omega_L)$$

Fitting this model, one can obtain the densities of the two species in the vapor. After mirroring the frequency axis to obtain increasing frequencies from left to

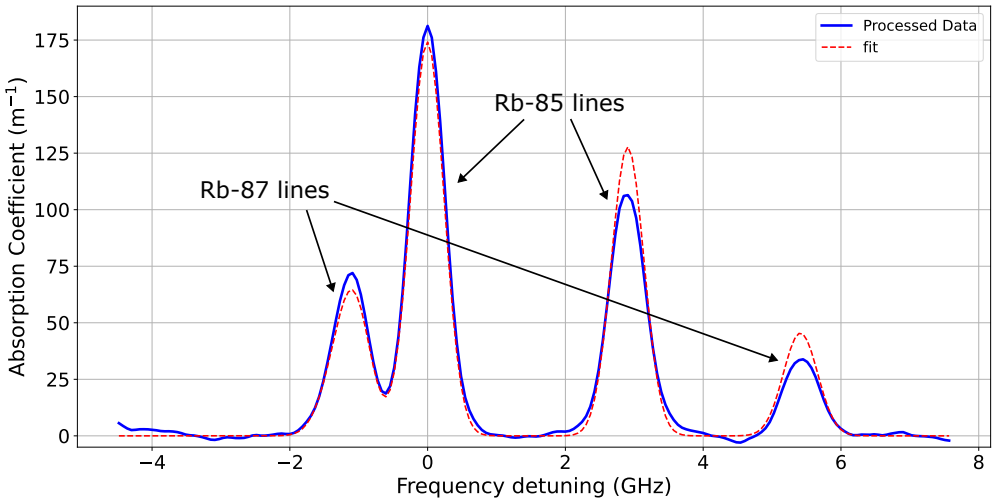

Figure 4.5: Fit of the theoretical absorption cross-section (red dashed line) to the experimental absorption coefficient (blue line) to extract the atom number density.

right (the laser scan data consisted of half a triangular wave period, with frequency decreasing over time), the theoretical model is also used to calibrate the frequency

axis of the acquired spectra. The zero of the frequency axis is set arbitrarily to coincide with the maximum of absorption (corresponding to the $|5^2S_{1/2}, F_g = 3\rangle \rightarrow |5^2P_{3/2}, F_e = 2,3,4\rangle$ ^{85}Rb unresolved transitions).

4.1.2 Cell dynamics

By performing the above analysis on the series of spectra acquired during the activation process for each cell, one can track the evolution of the atom number density n over time. This allows not only to quickly identify faulted cells, but also to study the dynamics of the Rubidium vapor pressure inside the microcells after the activation laser is turned off, and possibly link it to the microchannel width and geometry. In **Figure 4.6** the comparison between the activation dynamics of

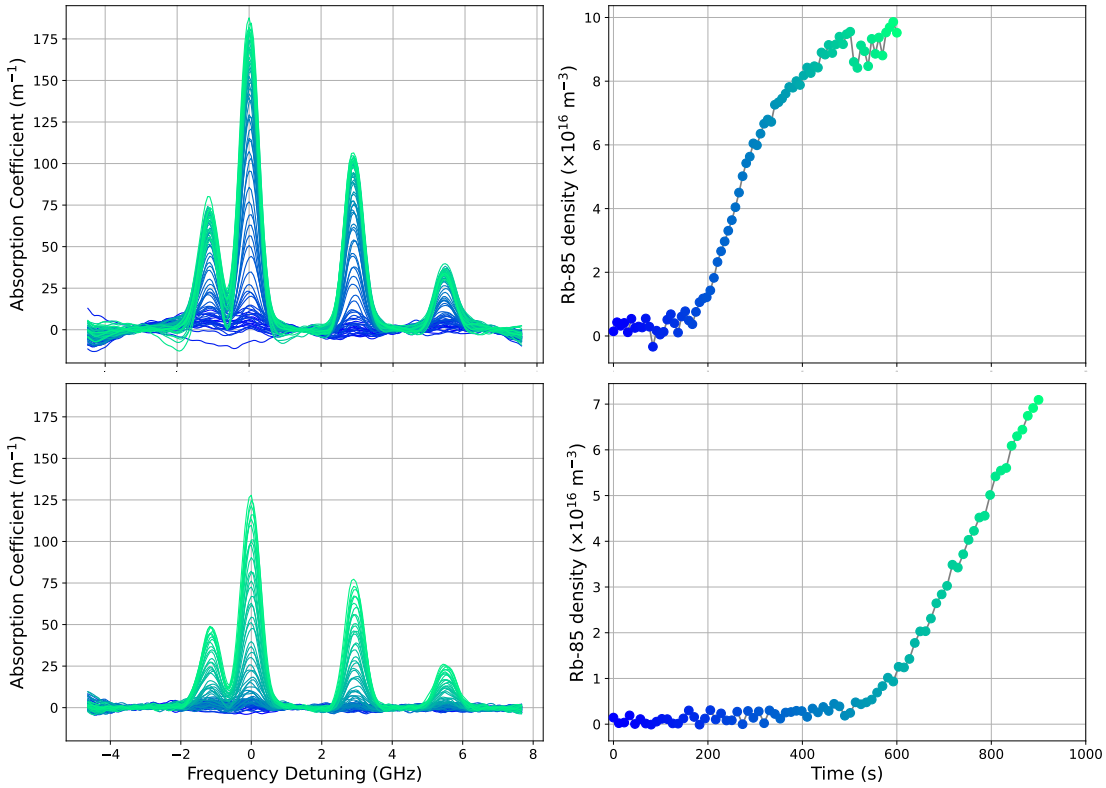

Figure 4.6: Signal increase and evolution of the atom number density during the filling process for microcells with 40 µm (top) and 20 µm (bottom) wide microchannels. Left: absorption spectra acquired from earlier (blue) to later (green) times, starting from the closure of the high-power laser shutter; Right: total number density evaluated by fitting the absorption profiles at each time step.

cells exhibiting different microchannel widths is depicted. The high-power laser is

turned on for 4 s to activate the microdispensers, and the acquisition starts from the moment it is turned off. As one can expect, wider microchannels lead to faster stabilization of the vapor pressure, in that they allow for a more efficient diffusion of the Rubidium atoms from the reservoir to the optical cavity. Narrower channels, on the other hand, restrict the flow of atoms and result in longer stabilization times. Cells for which the microchannels have collapsed, resulting in a wide "tunnel" connecting the two cavities, show a very fast filling dynamics. Such rapid filling

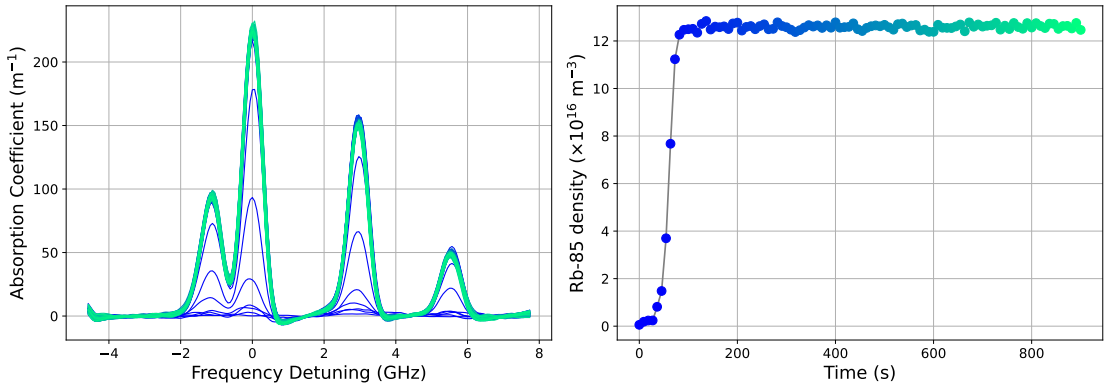

Figure 4.7: Signal increase and evolution of the atom number density during the filling process for a microcell with collapsed microchannels.

(**Figure 4.7**) is not necessarily a good sign, as cells with collapsed channels often exhibit poor optical quality. This is likely due to the fact that the collapse of the channels can introduce contaminants or defects in the cell, which can introduce line broadening and affect the two-photon absorption spectra and overall performance and durability.

Rubidium vapor pressure analysis

A final scan of all the cells was performed 2 hours after activation, as a conclusive assessment of the activation dynamics. After 10 days from activation, during which the batch was left at ambient temperature, all the activated cells were tested again for a sanity check before dicing. The analysis was performed by heating the cells again to 67 °C and acquiring new Doppler spectra. To check if a cell is in the regime of saturation, the parameter to be extracted is the vapor pressure of Rubidium inside of it. The atom number density of the Rubidium vapor inside the microcells can be directly linked to its vapor pressure through the ideal gas law $P = N/V \cdot k_B T = n k_B T$. Knowing that inside the apparatus in **Figure 4.2** the cells are heated at 67 °C (340 K), one can compare the measured vapor pressure to the expected one to understand if the system has reached equilibrium.

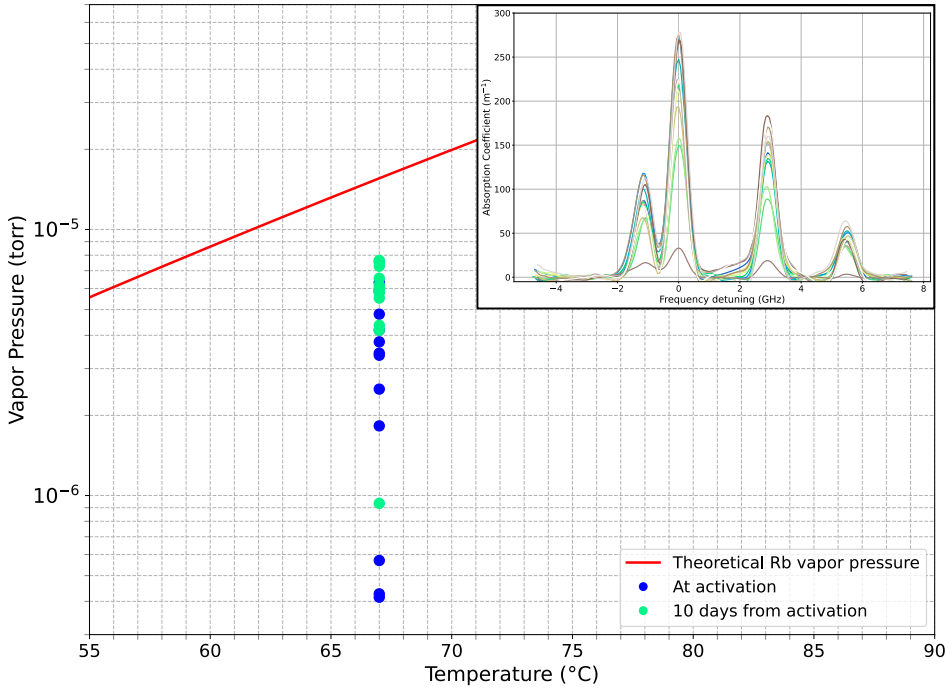

Figure 4.8: Measured vapor pressure of Rubidium in each cell after activation (blue dots) and after 10 days from activation (green dots), compared with the expected theoretical curves from [56] at 67 °C (red line). The values of pressure are obtained summing the partial pressures of the two Rubidium isotopes. The inset shows the absorption spectra of all the cells after 10 days from activation, before dicing

The pressures extracted from measurements after 2 hours and after 10 days from activation are shown in **Figure 4.8**, where each value of pressure is obtained by summing the partial pressures of the two isotopes of Rubidium, ^{85}Rb and ^{87}Rb, extracted from the atom number densities of the two species from the absorption spectra fittings. An increase and stabilization in pressure is visible. Most of the cells in figure, except the evidently faulted ones, show a vapor pressure close to the expected value, but usually smaller by about a factor two. This discrepancy can be attributed to various reasons, such as inaccuracies in the temperature control, small errors introduced during the signal post-processing and the fitting procedure of the model (which being based on Beer-Lambert law affects exponentially the estimation of n), or a possible inadequacy of the model itself for the laser powers in use during the measurements (the Doppler spectra were derived assuming low optical power, so that the atomic levels and the population of atoms are unperturbed, but this is not necessarily the case even for intensities below the saturation intensity, see

[57]). Most importantly, though, this discrepancy may signal that the vapor inside the microcell has not reached equilibrium yet, and that a longer waiting time after the activation process is required to allow the Rubidium atoms to fully diffuse and stabilize their pressure inside the optical cavity.

4.2 Two-photon setup

In order to separate the cells, the wafer was cooled down to room temperature and removed from the automatic setup; then it was diced through the use of a diamond saw, obtaining the single microcells. Once the individual microcells have been obtained by cutting the wafer, one of them can be mounted on the rack-scale two-photon clock setup. Such setup is designed to probe the two-photon transition $|5S_{1/2}, F = 2\rangle \rightarrow |5D_{5/2}, F = 4\rangle$ of Rubidium at 778 nm and lock the laser frequency to it, thus creating an optical atomic frequency reference that can be subsequently sent to a frequency comb for down-conversion to RF frequencies and then to an electronic counter that creates the clock. The system in **Figure 4.9** is

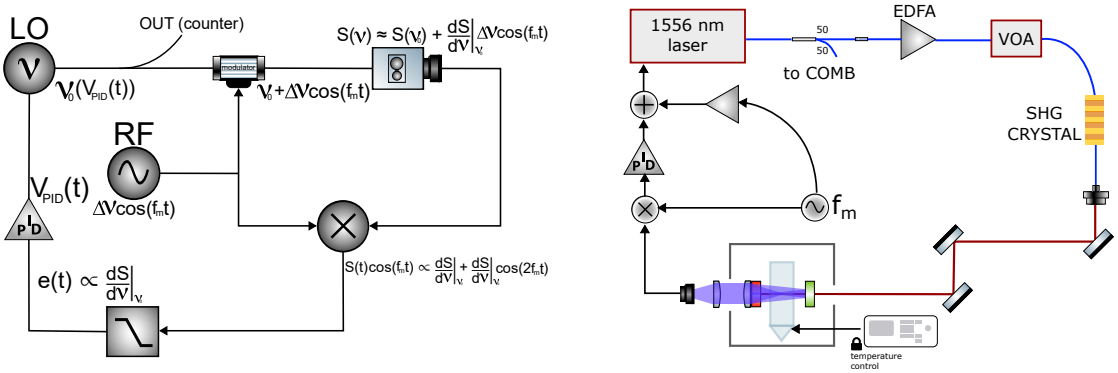

Figure 4.9: Schematic of a generic Frequency Modulated (FM) atomic clock (left) and of the actual implementation scheme used in this work (right), comprised of temperature stabilization loop, frequency modulation through direct laser piezo modulation, fluorescence detection through a PMT, and frequency stabilization through a lock-in amplifier. The 778 nm light is generated through second harmonic generation (SHG) from a telecom 1556 nm laser source.

ultimately used to lock the laser frequency to a specific atomic transition, creating the actual clock. However, when operated in open loop and with a triangular-wave modulation of the laser frequency, it simply reduces to a two-photon spectroscopy setup used to investgate the atomic transitions. The laser source is a commercial telecom fiber laser operating at 1556 nm, whose output is frequency-doubled through second harmonic generation (SHG) in a periodically-poled lithium niobate

(PPLN) waveguide crystal, resulting in about 30 mW of optical power at 778 nm. The laser frequency can be scanned by modulating the voltage of the piezo-electric crystal that stretches the laser substrate, which results in a change of the output wavelength due to the thermo-optic and electro-optic effects inside the laser cavity [54]. The free-space part of the optical setup consists of the 778 nm output beam, a beam splitter that sends, depending on light polarization, 1-10% of the optical power to a photodiode (PD) used to stabilize the input optical power through a control loop, an optical system that takes care of collimating and focusing the beam, and the physics package containing: an oven that encloses the microcell and brings the Rb vapours to the desired vapour pressure through heating at 100 °C, and two semi-reflective mirrors used to filter out the 778nm input light from the fluorescence in output and retro-reflect it to form the counter-propagating photon. The physics

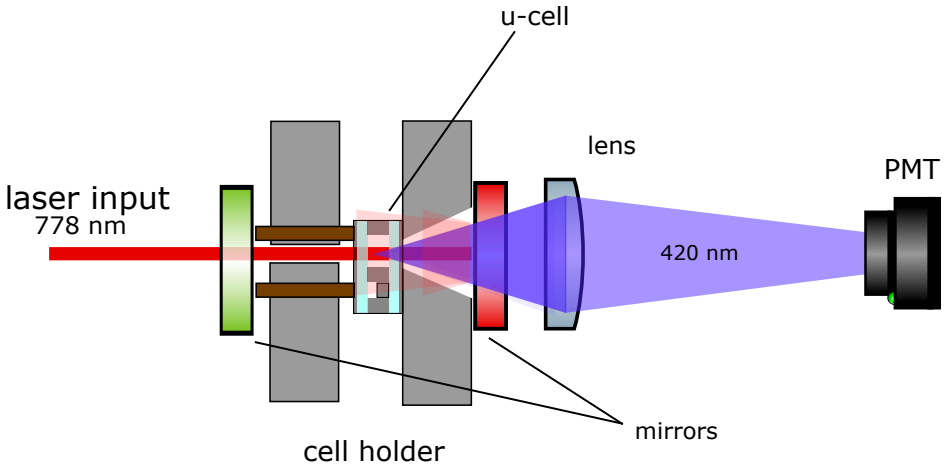

Figure 4.10: Physics package schematic showing the microcell inside the oven, the cell holder and the semi-reflective mirrors for fluorescence detection and retro-reflection of the beam. The fluorescence signal is collected at the PMT.

package in **Figure 4.10** is then followed by a photomultiplier tube (PMT) to read the 420 nm fluorescence signal resulting from the spontaneous radiative relaxation of the Rb atoms following the two-photon excitation. This setup is not suited to perform wafer-scale characterization, and changing the cell under analysis requires manual intervention, cooling down the oven, opening the physics package and re-aligning the optics. In order for the two-photon absorption to take place with a reasonable efficiency, proper alignment, collimation and focusing of the light beam are required. The former two are necessary so that the incident and reflected photons are low-divergent, well overlapped and co-linear which, together with the temporal coherence provided by the laser light, are essential ingredients to achieve two-photon absorption. The latter aims at having the optical power be concentrated in the smallest area (spot) possible, and thus retain the strongest

possible signal. The optimization of the optical system was carried out in two steps: at first, the optics consisted of a simple collimator, two mirrors and a telescope made up of two-lenses, whose distance was adjusted to properly focus the beam; as the performances were not satisfactory even after optimization, the optical system was subsequently upgraded to become a single component: a new collimator with built-in adjustable optics, directed straight into the physics package. At the same time, along the fiber line, the SHG duplication crystal was substituted with a new, more efficient one. The cell quality and line broadening contributions from various physical effects will be discussed upon measurements, and the improvement in the spectroscopic signal will be demonstrated comparing measurements on the same cell with the different experimental configurations.

4.2.1 Setup optimization

Two-photon absorption is a non-linear process, meaning that the probability of an atom to absorb two photons simultaneously is not proportional to the intensity of the incident light, but to its square (see **Section 2.2.2**). This means that, in order to have a reasonable efficiency of the process, high optical intensities are required. Since the available optical power at 778 nm is limited (about 30 mW), it is necessary to concentrate it in the smallest possible area (spot) in order to reach high intensities. This is achieved by collimating and focusing the laser beam using a telescope made of two lenses. The collimation process consists in reducing the divergence of the beam, so that it remains as collimated as possible along the optical path, and then focusing it at the position of the microcell containing the Rubidium vapors. The very first step is always profiling the beam, by performing measurements of the laser spot at different positions along its propagation axis through a CCD beam profiler, in order to obtain its waist position and radius. Then, one can calculate the properties of the beam after propagation through an optical system by means of gaussian beam theory and the ray transfer matrix method, and use the optics to manipulate and focus it in the desired locations.

Setup 1

In the first setup, alignment is taken care by acting on the mirrors' orientation, checking how well the retroreflected beam superimposes to the incident one. Collimation and focusing is taken care of by the telescope, made up of two lenses (a diverging and a converging one, with focal lengths respectively of 100 mm and -50 mm). Knowing the properties of the two lenses, such as their focal length and magnification, and measuring the properties of the unfocused beam along the optical path with a beam profiler, one can use gaussian beam optics and the ray transfer matrix method to compute the optimal distance between them so that the

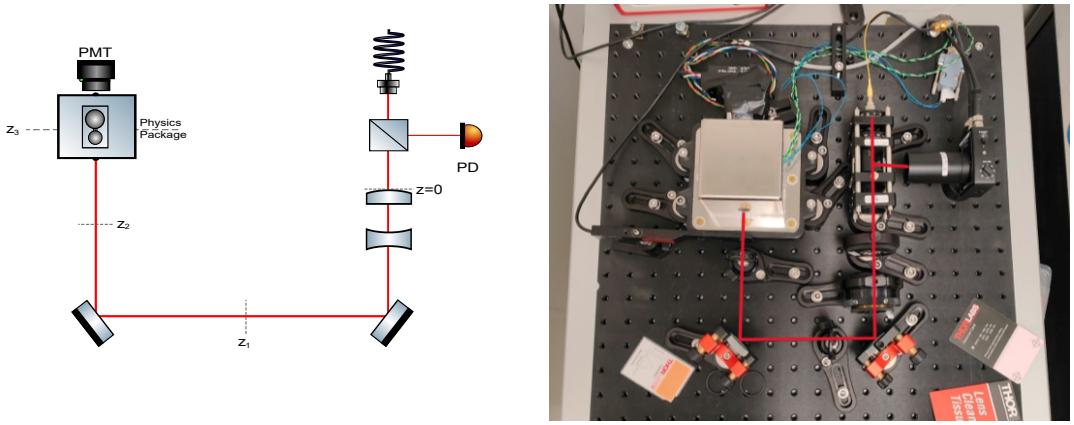

Figure 4.11: Schematic of the first free-space setup. The light source emits a beam that is collimated using a two-lenses telescope. The collimated beam is then directed towards physics package.

spot of maximum intensity (beam waist) falls exactly on the microcell in position z_3 (see scheme in **Figure 4.11**).

Measuring the beam waist radius and position Assuming normalized intensity $I_0 = 1$, and since the beam is not centered at the origin of the $x - y$ coordinate system of the beam profiler but at a generic r_0, the fitting function will be the shifted gaussian:

$$I(r, z) = \exp\left(-\frac{2(r - r_0)^2}{w^2(z)}\right) + c \tag{4.1}$$

At a known z, the fitting parameters will be $w(z)$, r_0, and c, where c is a constant accounting for the measurement instrument's offset. An example of such kind of measurement and gaussian fit is shown in **Figure 4.12**. Measuring the variance of the gaussian profile at different z positions along the optical path, one can evaluate where the beam's waist falls, and then use the lenses to move it along the path so that it is as close as possible to the location of the microcell (or at least so that the cell falls in the Rayleigh range of the laser beam), meaning that the beam is properly focused and collimated. The intensities along the x and y directions are treated independently, since the model assumes cylindrical symmetry about the propagation axis, even though a more careful analysis employing a proper 2D gaussian accounting for an elliptical spot shape could provide information about astigmatism, which is neglected here. Once a direction (x or y) is chosen, and being $w_1 = w(z_1)$ and $w_2 = w(z_2)$ known from the gaussian fits, one can use the expression of the beam width at a generic position in terms of the beam waist from

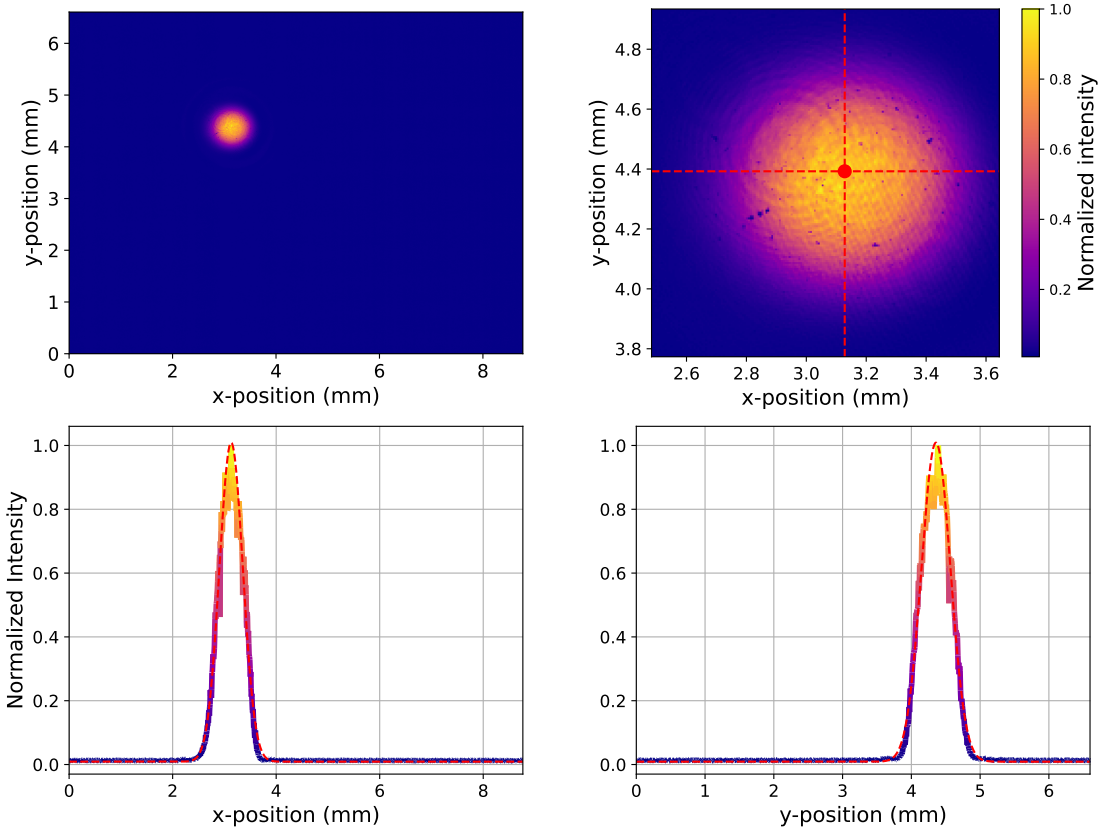

Figure 4.12: Top: beam profiling; Bottom: cuts (solid lines) and gaussian fits (dashed lines) along the x and y directions at the point of maximum intensity. The coordinate system is that of the beam profiler's window

Section 2.1 to retrieve w_0 and z_0 by numerically solving the non-linear system:

$$\begin{cases} w_1 = w_0\sqrt{1+\left(\dfrac{z_1-z_0}{z_R}\right)^2} \\ w_2 = w_0\sqrt{1+\left(\dfrac{z_2-z_0}{z_R}\right)^2} \end{cases} \tag{4.2}$$

where the Rayleigh range z_R also depends on w_0. Two values of z_0 and w_0 will be obtained for the two directions. The difference between these values can be an indication of how astigmatic the beam is.

Calculation of the beam parameters The beam can be manipulated by acting on the telescope lenses. To calculate what the distance between the lenses must be in order to put the beam waist at the position of the cell z_3, the ray transfer matrix

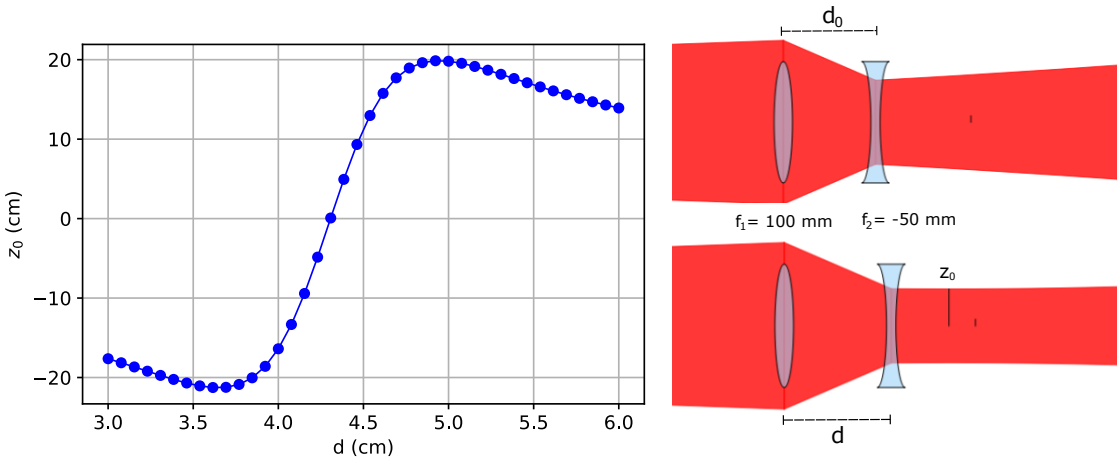

Figure 4.13: Left: beam waist position z_0 as a function of the distance between the two lenses d; Right: graphical representation of the beam shape through the optical system before (top) and after (bottom) the collimation. A negative z_0 indicates that the beam is diverging.

method was applied (see **Section 2.1**). First, the complex beam parameters at positions z_1 and z_2 are obtained using the previous data from the fits:

$$q_1 = q(z_1) = z_1 - z_0 + iz_R$$

$$q_2 = q(z_2) = z_2 - z_0 + iz_R$$

If one chooses z_1 as the output plane of the optical system, the ABCD matrix will be the product of the matrix associated with lens 1, the matrix associated with free-space propagation for a distance d_0 (the initial distance between the two lenses), the matrix associated with lens 2, and the matrix associated with free-space propagation for a distance d_1 (the distance between lens 2 and position z_1). The expressions of the matrices for all such optical components are found in [28]. To find the input beam parameter q_{in} starting from the output one q_1, one can invert **Equation 2.3** having:

$$q_{\text{in}} = q(0) = \frac{Dq_1 - B}{-Cq_1 + A}$$

where A, B, C, D are the entries of the overall ray transfer matrix of the system (at the fixed d_0 distance between the lenses), obtained by multiplying the matrices of each individual element in the order they are encountered by the beam. Once the beam parameter at the input of the system is known, it is possible to calculate the beam parameter at the output of the system for any distance d between the two lenses by propagating forward once again, and using the proper ABCD matrix (which now becomes a function of the distance d between the lenses). A curve

representing the waist position z_0 as a function of d can be plotted (**Figure 4.13**), and the optimal distance d_{opt} that places the waist at the desired position $z_3 = 38.25$ cm (the location of the microcell) can be found by solving the equation $z_0(d) = z_3$. Unfortunately, in our case this equation does not have any solution: as one can see from the figure, with the present lenses the farthest distance where the waist can be put is about 20 cm, which is still smaller than the position of the cell. Furthermore, the physical limitations of the telescope didn't allow to reach such distance, as the maximum separation between the lenses allowed by the system is 4.45 cm. It was nonetheless possible to at least take the physics package into the Rayleigh range of the beam, so that the intensity of light at the cell is still increased. Further beam profiling measurements were taken after adjusting the telescope to the maximum possible lens distance, confirming that the waist position had moved closer to the cell. The results are summarized in **Table 4.1**. Measures of the

	Before	After
Lenses distance (d)	4.10 cm	4.45 cm
Waist position (z_0) with respect to $z = 0$	-12.24 cm	9.86 cm

Table 4.1: Beam focusing and collimation results. After the optimization, $z_3 = 38.25$ cm is now (barely) within the Rayleigh range of 36.34 cm from the beam waist z_0

spectral lines provide information about the quality of the signal to be used for the atomic clock, and thus about the quality of the microcell itself. The narrower and more intense the lines are, the better the cell is, since the linewidth and intensity of the atomic signal will have a direct effect on both the atomic quality factor and on the signal-to-noise ratio. In **Figure 4.14** the spectrum acquired with Setup 1 from cell A1/4 (10 µm channel width) is shown, along with the Lorentzian fit used to extract the linewidth.

Setup 2

In the new setup, the whole system of optics (telescope and mirrors) was replaced by a single collimator with built-in focusing optics and 5 degrees of freedom (Pitch,Yaw and xyz translation axes) to facilitate alignment. The collimator is directly pointed at the physics package, thus simplifying the optical path and reducing the number of optical components. The beam resulting from the new collimator was profiled using the same techniques presented in the previous paragraph, and focused at the exact position of the cell ($z_2 = 10.5$ cm in **Figure 4.15**). The alignment was taken care by acting on the additional degrees of freedom available from the collimator stand. These new components provided a beam with an already much smaller

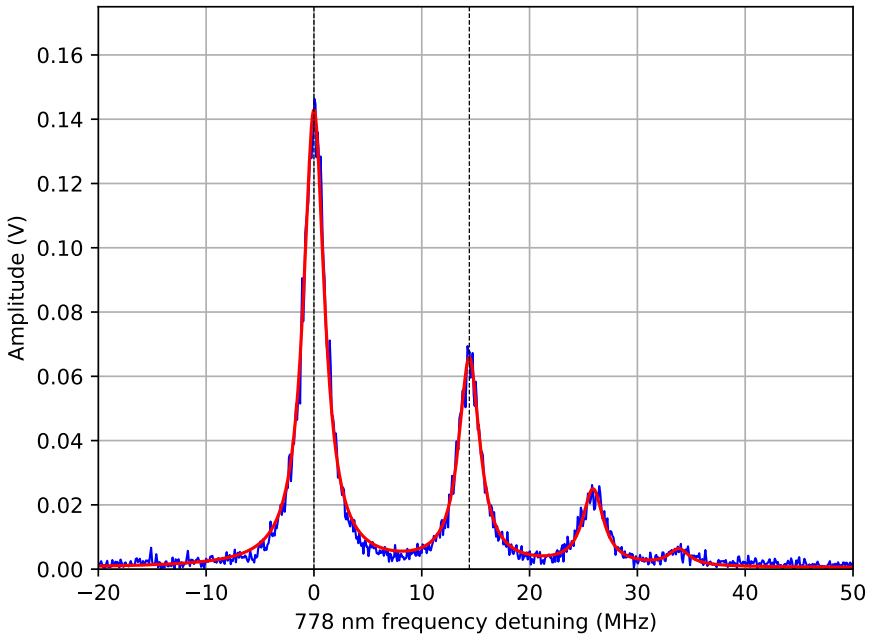

Figure 4.14: Two-photon spectroscopy fluorescence signal acquired with Setup 1 from the A1/4 cell, showing the Doppler-free $|5S_{1/2}, F = 2\rangle \rightarrow |5D_{5/2}, F = 4,3,2,1\rangle$ ^{87}Rb transitions. The $|5S_{1/2}, F = 2\rangle \rightarrow |5D_{5/2}, F = 4\rangle$ transition (leftmost peak) exhibits a linewidth of 2.35 MHz

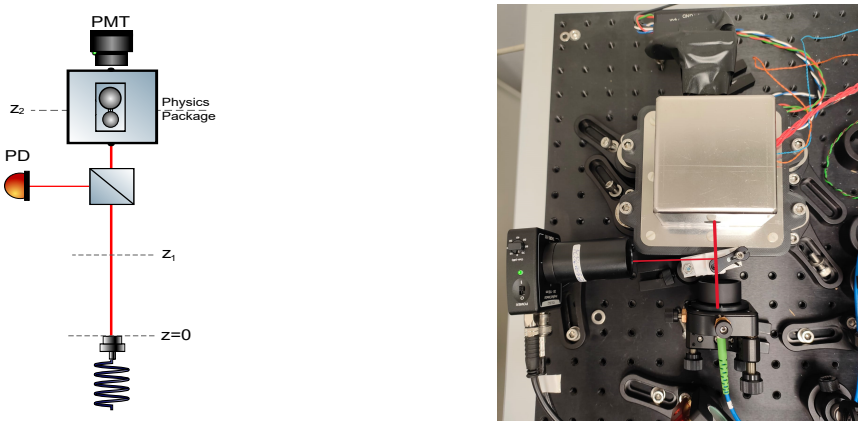

Figure 4.15: Schematic of the ugraded free-space setup. The collimator contains the focusing optics and is directly pointed at the physics package

waist radius of 134.4 µm and a resulting Rayleigh range of 7.30 cm. This new setup is thus simpler, more compact and better performing than the previous one. In **Figure 4.16** the beam profiling measurements and gaussian fits for the new

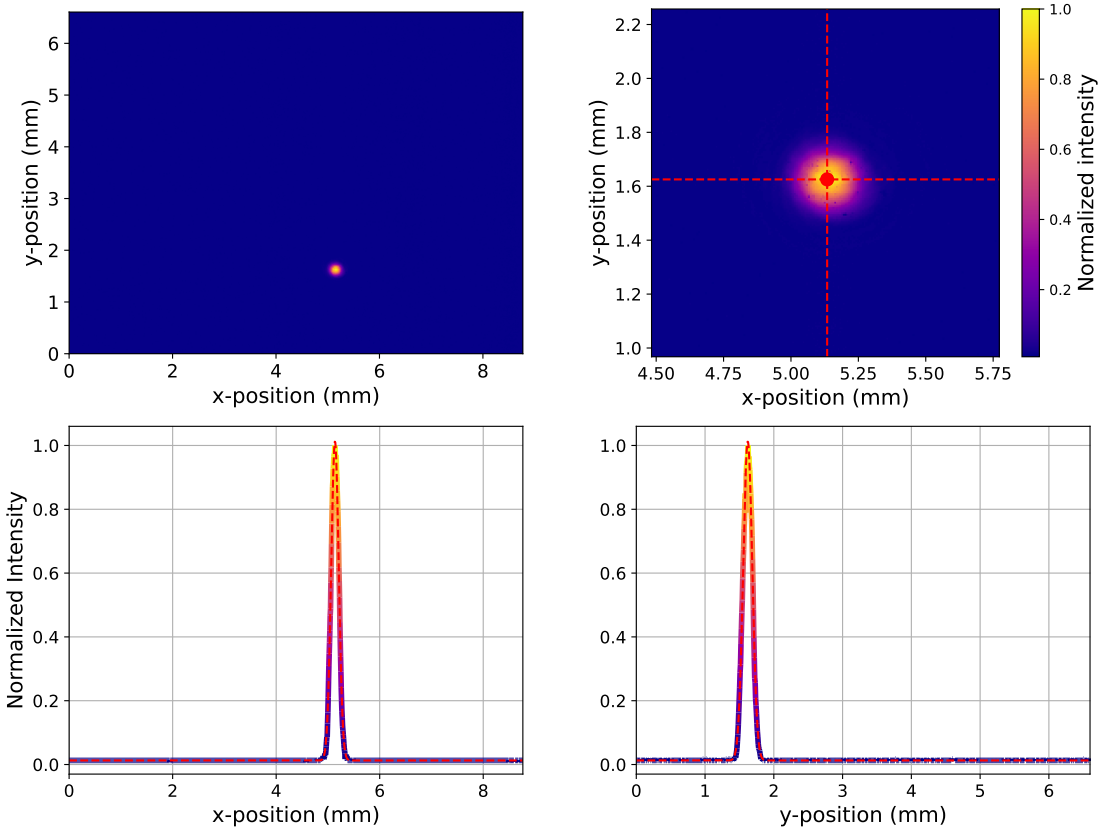

Figure 4.16: Top: beam profiling; Bottom: cuts (solid lines) and gaussian fits (dashed lines) along the x and y directions at the point of maximum intensity. The coordinate system is that of the beam profiler's window. The measurement was taken at a distance of 10.5 cm from the collimator.

setup are shown, confirming the smaller waist radius and thus higher light intensity at the cell. Since the fluorescence signal amplitude depends on the square of the intensity, a significant increase in signal is expected. In **Figure 4.17** the spectrum acquired with Setup 2 from cell A1/4 (10 µm channel width) is shown, along with the Lorentzian fit used to extract the linewidth. Compared to the previous setup, a reduction in linewidth of about 810 kHz is observed, along with an increase in signal of more than 6 times in amplitude (see comparison with **Figure 4.14**).

Signal improvement assessment and cell evolution

With the new setup the amplitude of the signal is increased, as the laser beam is more focused and the waist radius is decreased. The signal itself, however, also depends on the density of Rubidium inside the cell, which may have changed from

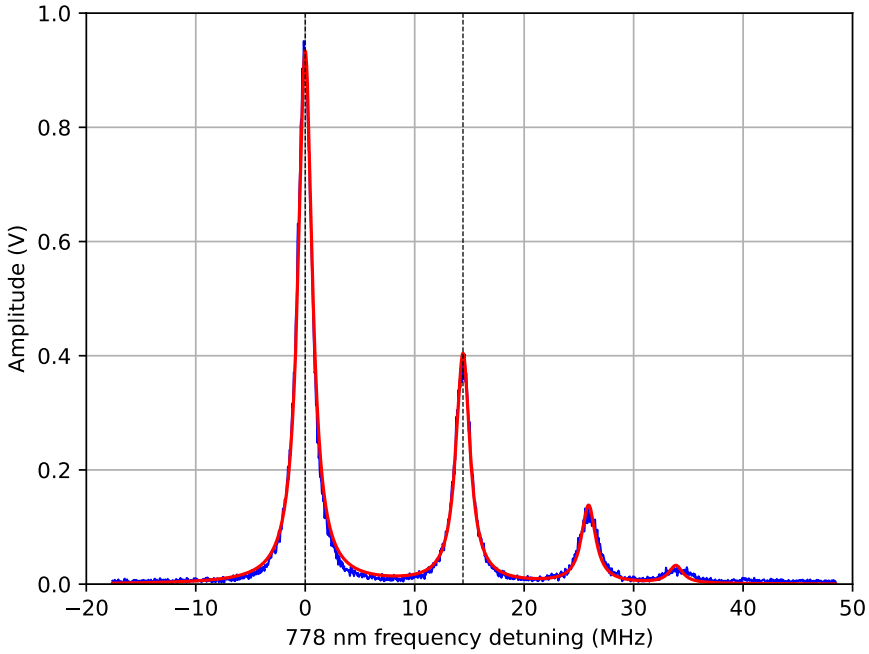

Figure 4.17: Two-photon spectroscopy fluorescence signal acquired with Setup 2 from the A1/4 cell, showing the Doppler-free $|5S_{1/2}, F = 2\rangle \rightarrow |5D_{5/2}, F = 4,3,2,1\rangle$ ^{87}Rb transitions and Lorentzian fit of the lines. The $|5S_{1/2}, F = 2\rangle \rightarrow |5D_{5/2}, F = 4\rangle$ transition (leftmost peak) exhibits a linewidth of 1.54 MHz

one measurement to the other. Indeed, a first measurement of the Rb density in the cell was performed at the automatic setup through Doppler spectroscopy before cutting the wafer. The microcell was then cooled down to room temperature, cut from the wafer and introduced in the physics package of the two-photon setup, where it was brought to 100 °C and measured using Setup 1 to obtain the spectrum in **Figure 4.14**. Assuming the Rubidium number density n has not changed in the cell after cooling and heating back up, the vapor pressure is only dependent on the new temperature and $n_{Doppler} = n_{two\,photon}$. The measurement with Setup 2 was performed after 10 days of the cell being kept at 100°C while changing the optics, which may have resulted in a further evolution of the vapors inside, and possibly an increase of the density. By comparing the spectra acquired with Setup 1 and Setup 2, it is possible to calculate the increase in atom number density between the two measurements (if any). In order to understand if and how much this effect has had an impact, we should compare the actual signals (not just the amplitudes) among the measurements. The intensity of the signal is calculated as the area of

the Lorentzian peak. For a Lorentzian of the form:

$$L(\omega_L) = A\frac{(\Gamma/2)^2}{\omega_L^2 + (\Gamma/2)^2}$$

the area (the signal) is:

$$S = \frac{\pi}{2}A\frac{\Gamma}{2}$$

But also, up to fixed constants, the signal strength depends on:

$$S \propto I^2 \cdot n$$

where I is the beam intensity and n is the Rubidium density. So, for two signals S_1 and S_2, their ratio is:

$$\frac{S_2}{S_1} = \left(\frac{I_2}{I_1}\right)^2 \cdot \frac{n_2}{n_1}$$

and the increase in Rubidium density between the two measurements can be obtained as:

$$\frac{n_2}{n_1} = \left(\frac{I_1}{I_2}\right)^2 \frac{S_2}{S_1} = \left(\frac{I_1}{I_2}\right)^2 \frac{A_2\Gamma_2}{A_1\Gamma_1} \tag{4.3}$$

Since in the two measurements the beam waist changes and the applied optical powers are also slightly different, the intensity in the two cases can be calculated as:

$$I = \frac{2P}{\pi w_0^2}$$

with P the optical power and w_0 the beam waist. The parameters of the two measurements are summarized in **Table 4.2** Using **Equation 4.3** one can estimate,

	Setup 1	Setup 2
Beam waist (w_0)	300.0 µm	134.4 µm
Optical power (P)	15.5 mW	15.0 mW
Peak amplitude (A)	0.14 mV	0.93 mV
Linewidth (Γ)	2.35 MHz	1.54 MHz

Table 4.2: Signal parameters for the different measurement setups on the same cell

from the second measurement, a Rb density increase in the optical cavity of about 1.85 times. This effect is shown in **Figure 4.18**, where the pressure extracted from the atom number density measured with Doppler spectroscopy at the automatic

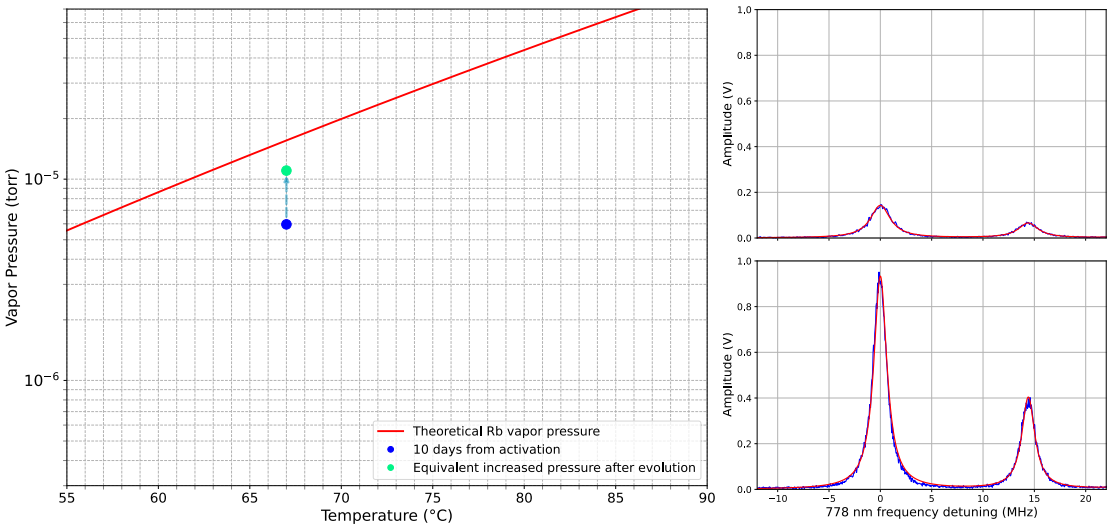

Figure 4.18: Left: comparison between the vapor pressure measured 10 days after activation (blue) and the equivalent value obtained by multiplying it by the density increase after 10 days at 100 °C in the two-photon setup (green); Right: signal comparison between Setup 1 (top) and Setup 2 (bottom). The measurements are from cell A1/4.

setup is compared to an equivalent value of pressure obtained multiplying it by the increase resulting from further cell evolution. The new value here recovered accounts for most of the underestimation of the vapor pressure, suggesting that a longer waiting time after activation is indeed required to reach equilibrium inside the microcells. Further investigation on the duration of this "burn-in" period required by the cell to reach a saturated vapor condition can be the object of future work.

4.2.2 Discussion of the line broadening contributions

While for simplicity the spectral lines acquired with the two-photon setup were fitted with Lorentzian functions to extract their linewidth, in reality the line shape is more complex and is affected by various broadening mechanisms. A more accurate model for the line shape when the natural linewidth and the gaussian broadening are comparable is the Voigt profile, which is a convolution of a Lorentzian and a Gaussian profile, accounting for both homogeneous and inhomogeneous broadening mechanisms impacting respectively on the Lorentzian (Γ) and Gaussian (σ) contributions. The Voigt fit of the latest measurement of cell A1/4 is shown in **Figure 4.19**. Notice that the data is from the same measurement shown in **Figure 4.17**, but the Voigt profile better fits the lineshape, especially on the tails.

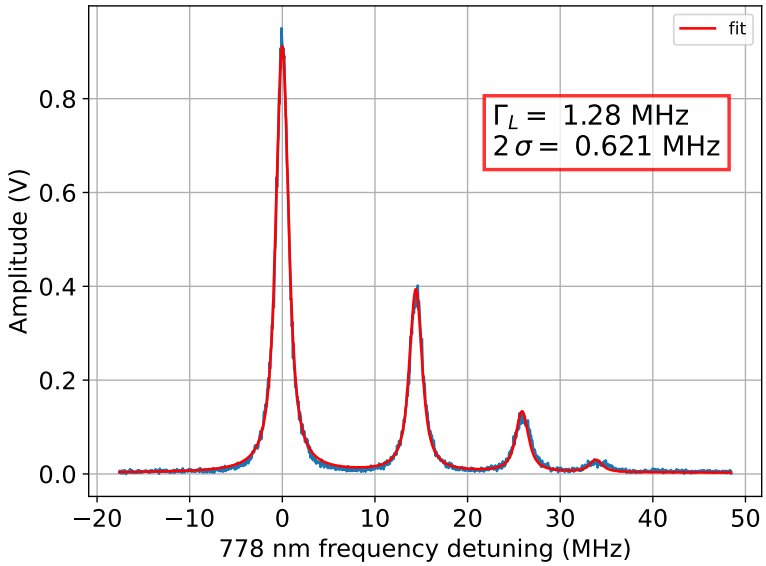

Figure 4.19: Voigt fit of the A1/4 cell two-photon spectrum acquired with Setup 2. The parameters extracted from the fit are a Lorentzian linewidth of $\Gamma = 1.28$ MHz and a gaussian linewidth of $2\sigma = 0.621$ MHz representing respectively the homogeneous and inhomogeneous contributions to the line broadening.

Both homogeneous and inhomogeneous broadening contributions are now discussed, linking them to the experimental conditions of the two-photon spectroscopy setup and the microcell properties.

Residual Doppler broadening due to imperfect alignment

Since the laser beam is manually aligned by acting on the mirrors (in the case of Setup 1) or on the collimator mount (in the case of Setup 2), a perfect overlap between the incident and retroreflected beams is hard to achieve. Any small angle θ between the two beams results in a residual Doppler broadening, since the two photons are no longer exactly counter-propagating, thus making the absorption sensitive to the atomic velocity along the bisector of the two beams. In **Figure 4.20** the alignment scheme is shown. The angle θ is obtained by considering the reported dimensions in figure, where the misalignment between the emitted beam and the retroreflected spot was consideed to be the minimum distance appreciable via bare-eye inspection of about 0.5 mm. The resulting broadening in terms of FWHM can be obtained using **Equation 2.16**, at a temperature of 100 °C and using the $|5S_{1/2}, F = 2\rangle \rightarrow |5D_{5/2}, F = 4\rangle$ transition frequency. The resulting broadening is

$$\Delta f_{RD} = 3.26 \text{ kHz}$$

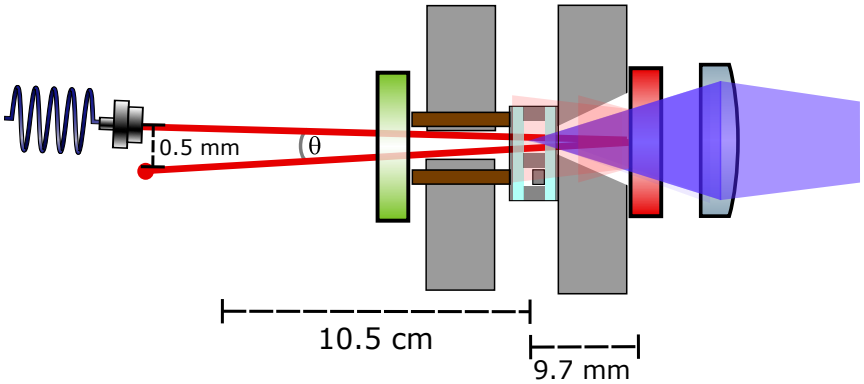

Figure 4.20: Alignment scheme of the laser beam on the microcell. An angle θ between the incident and retroreflected beams results in a residual Doppler broadening of the two-photon transition.

which turns out to be negligible compared to the gaussian broadening $2\sigma = 621$ kHz from **Figure 4.19**.

Transit time broadening

Transit time broadening arises from the finite time an atom spends in the interaction region with the laser beam. For two-photon spectroscopy, it can be estimated using **Equation 2.17** with $w_0 = 134.4$ m is the beam waist radius. Using the parameters of Setup 2, the resulting transit time broadening is

$$\Delta f_{TT} = 526.78 \text{ KHz}$$

which is a significant contribution to the overall Gaussian broadening observed. The inverse dependence on the beam waist suggests that two opposing effects are present when trying to optimize the beam focusing: on one hand, a smaller waist increases the light intensity and thus the two-photon absorption efficiency (which goes as the square of the light intensity), but on the other hand it also increases transit time broadening, which degrades the spectral line quality. A trade-off must be found when optimizing the clock performance.

Zeeman broadening

After the evaluation of transit time and imperfect alignment Doppler broadening contributions, if one assumes that no other inhomogeneous broadening mechanisms are present, the remaining Gaussian broadening can be ascribed in its entirety to Zeeman broadening. Assuming all inhomogeneous contributions are statistically independent and additive in quadrature (their variances add), the Zeeman

broadening can be estimated, in terms of FWHM, as:

$$\Delta f_Z = 2\sqrt{2\ln 2}\sqrt{\sigma^2 - \left(\frac{\Delta f_{TT}}{2\sqrt{2\ln 2}}\right)^2 - \left(\frac{\Delta f_{RD}}{2\sqrt{2\ln 2}}\right)^2} = 507 \text{ kHz}$$

The contribution seems rather small, but new setups aimed at higher performances could nonetheless benefit from the addition of magnetic shielding around the physics package to further reduce this effect.

Homogeneous mechanisms, collisional broadening and cell quality

As the Gaussian contribution to linewidth was discussed and ascribed to the above mechanisms, the Lorentzian contributions to broadening contained in the Γ parameter of the fit in **Figure 4.19** are now tackled. Knowing that the natural linewidth of the $|5S_{1/2}, F = 2\rangle \rightarrow |5D_{5/2}, F = 4\rangle$ ^{87}Rb transition is about $\Gamma_{Natural} =$ 330 kHz [58, 40], and considering homogeneous mechanisms to be the direct sum of independent transition rates, the collisional broadening contribution can be estimated as:

$$\Delta f_{Collisional} = \Gamma - \Gamma_{Natural} = 950 \text{ kHz}$$

The reduction of this contribution is a direct indicator of the quality of the microcell, as it depends on the presence of impurities and on the surface quality of the cell walls. Further investigation on the dependence of collisional broadening on the channel width and fabrication parameters of the microcells can be the object of future work.

Chapter 5

Conclusions and future prospects

In this thesis, I have presented the development and first characterization of microfabricated pill-based MEMS Rubidium microcells for a compact two-photon optical clock. The work was motivated by the increasing need of portable, low-SWaP frequency references that remain compatible with microfabrication and wafer-level integration, while at the same time approaching the performance of state of the art, lab scale optical standards. In this framework, the use of warm-vapor cells and two-photon Doppler-free interrogation schemes are particularly attractive. Critically, they rely on robust microcells with controlled vapor pressure and inert environment. This thesis, therefore, addressed both the technological realization of such microcells and their spectroscopic assessment in conditions relevant to clock operation.

On the fabrication side, a top-down process was established on 1 mm-thick silicon wafers, exploiting ICP-DRIE pattern transfer to form the passing cavities. Using the well known Bosch process, this allowed to achieve high aspect ratio etch structures. Anodic bonding was then used to form the 3D glass-silicon-glass hermetic structure and create the microcells. All the process steps described in this work were studied and optimized to reach the desired result, starting from image-reversal photolitography up to the KOH post-etch treatment used to mitigate DRIE sidewall scalloping with the aim of avoiding the formation of preferential condensation sites for alkali atoms. The microcells, with total dimensions of 4×7 mm after dicing, have a structure exhibiting two through-silicon passing cavities connected by thin microchannels: the smaller cavity acts as reservoir for the Rubidium solid precursor, consisting of a pill less than 1mm in size, while the larger one is devoted to the spectroscopic interrogation of the atomic vapours. Different microchannel widths were also studied, in order to investigate their structural resistance throughout the fabrication process and their effect on Rb vapors equilibration after precursor pill activation.

At wafer level, the pill microdispensers were activated with a focused 1111 nm

laser, and the evolution of the D_2 line absorption spectra was monitored in time. From fits to a theoretical absorption model, the densities of ^{85}Rb and ^{87}Rb were extracted and correlated with microchannel design. Wider channels led to a faster approach to steady-state vapor pressure, whereas narrower ones showed slower equilibration; cells exhibiting collapsed channels had a quick filling dynamics, but often showed a degraded optical quality. A comparison of measurements taken at activation and ten days after activation revealed a gradual evolution of the vapor pressure towards the expected saturated-vapor curve, with an initial underestimation of about a factor of two. This behaviour suggests a further investigation of the "burn-in" period before the internal atmosphere reaches equilibrium.

In the second part of the work, a selected microcell was integrated into a rack-scale two-photon setup at 778 nm, with fluorescence detection at 420 nm. Starting from a free-space telescope and mirror configuration, Gaussian beam analysis revealed the limitations in placing a sufficiently small waist at the cell position. This motivated an upgrade of the optics to a single collimator with integrated focusing and multiple degrees of freedom. Beam profiling confirmed a significant reduction of the waist at the cell (from $\approx$ 300 µm to $\approx$ 134 µm) and a corresponding increase in intensity. With this new optimized configuration, the $|5^2S_{1/2}, F = 2\rangle \rightarrow |5^2D_{5/2}, F = 4\rangle$ two-photon transition linewidth in the representative cell narrowed from $\approx$ 2.35 MHz to 1.54 MHz, while the signal amplitude increased by more than a factor of six. Accounting for the measured increase in Rubidium density over ten days ($\approx$ 1.85 times) helped reconcile these results with the previous wafer level estimates of the vapor pressure, further confirming the slow evolution of the vapors after activation.

A Voigt analysis of the two-photon lineshape allowed the separation of homogeneous and inhomogeneous contributions. For the selected cell, the fit yielded a Lorentzian width of $\approx$ 1.28 MHz and a Gaussian width $2\sigma \approx 0.62$ MHz. The Gaussian term was attributed mainly to transit-time and Zeeman broadening, with residual Doppler effects expected to be negligible in the counter-propagating scheme used. Once the natural linewidth of the transition was subtracted, the remaining homogeneous contribution on the order of 1 MHz was interpreted as collisional broadening. This directly links the observed linewidth to the internal gas environment and to the quality of the microcell, showing that the fabricated devices already support MHz-level interrogation, while still leaving room for further reduction of collisional effects via cleaner and more optimized fabrication procedures.

Overall, the thesis demonstrates that the first batch of pill microdispenser-based MEMS microcells meets the requirements for integration in a two-photon Rubidium clock: they can be fabricated with a reproducible process, activated and screened at wafer level, and operated in a two-photon setup with narrow linewidths and

high signal-to-noise ratio. The work establishes also a coherent workflow that connects process parameters (microchannel geometry, KOH treatment, bonding stack) to figures of merit relevant for clock operation (filling dynamics, saturated vapor pressure, collisional broadening).

Based on this work, several future developments can be proposed. On the fabrication side:

- introduction of getter materials inside the pill reservoir to capture residual contaminants and reduce the pressure inside the cell;
- the adaptation of the process to microcells with different scopes, e.g. buffer-gas filled cells for quantum memories or optically pumped magnetometers;
- functionalization of the cell: anti-relaxation coatings to reduce wall-collision effects and extend atomic coherence times, anti-reflection coatings on the glass layers to reflect the incident spectroscopic beam and generate the second photon at cell-level, integration of micro-heaters and temperature sensors for local temperature control, and the deposition of gold rings or dots to create favored cold sites for Rubidium condensation, improving long-term stability;
- integration of the optical setup using silicon photonics platforms, waveguide lasers and microring resonators to obtain actual chip-scale devices;

Further statistics on the filling dynamics and spectroscopic performance of a larger number of cells would also be beneficial to better understand the reproducibility and yield of the fabrication process.

On the spectroscopy side, future improvements include:

- implementation of magnetic shielding and controlled bias fields, together with a fine optimization of beam waist and interrogation geometry, to reduce Zeeman and transit-time broadening;
- reduction of parasitic broadening effects through improved optical and mechanical design of the physics package;
- realization of a full clock demonstration, by locking a laser to the two-photon transition in a microcell and characterizing the resulting frequency stability and long-term drifts.

In these perspectives, the work presented here provides both a technological and a characterization framework on which following generations of microcells and physics packages for compact two-photon optical clocks (and other quantum devices) can be built.

Appendix A

Derivation of the etalon transmission function

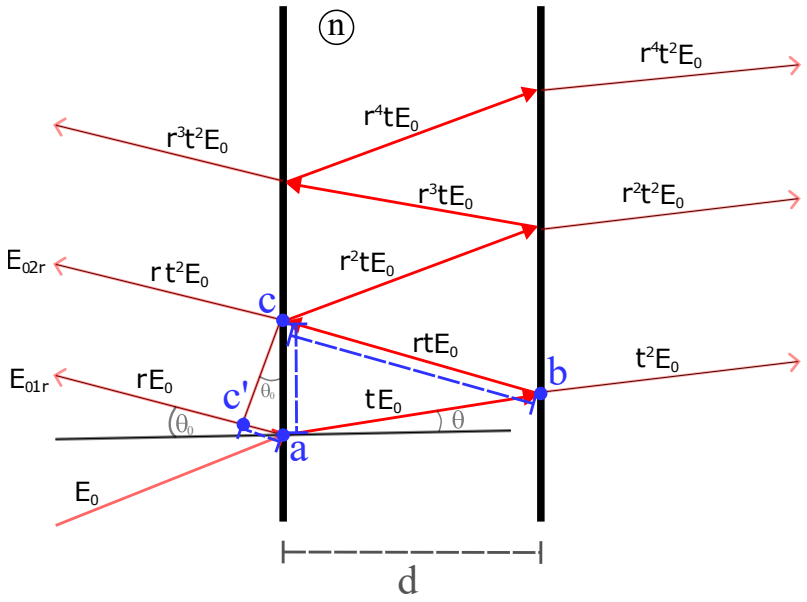

Figure A.1: Diagram of the etalon effect due to two parallel partially reflective surfaces. The input beam E_0 enters the etalon at an angle θ, in a medium with refractive index n between the two surfaces, and undergoes multiple reflections between the two surfaces separated by a distance d. The transmitted beams interfere coherently, producing the etalon effect.

The modulation of the spectroscopic signal due to the etalon effect can be modelled as follows. Assume a spectroscopic signal $S_0(\lambda)$ that would be measured in absence of etalon effects, i.e. a smooth function of the wavelength λ. The etalon effect introduces a wavelength-dependent transmission $T(\lambda)$, so that the measured signal will be

$$S(\lambda) = S_0(\lambda) \cdot T(\lambda)$$

A simple model can be derived for the transmission of a Fabry-Pérot cavity. Assume two identical, partially reflective, plane-parallel surfaces separated by a distance d, with no absorption losses. The medium between the surfaces has refractive index n (usually it will be air, $n = 1$), and each surface has reflectivity $R = |r|^2$, thus transmittivity $T_0 = 1 - R = |t|^2$. Light in general is refracted at an angle θ. When infinitely many reflections take place between the two mirrors, the output field will be the coherent sum of all the transmitted beams, one for each reflection. Assume an input field of amplitude E_0, then the transmitted field will be:

$$E_T = t^2 E_0 + r^2 t^2 E_0 e^{i\delta} + r^4 t^2 E_0 e^{2i\delta} + ... = E_0 t^2 \sum_{n=0}^{\infty} \left(r^2 e^{i\delta}\right)^n = E_0 t^2 \cdot \frac{1}{1 - r^2 e^{i\delta}}$$

where $\delta = \frac{4\pi n d \cos\theta}{\lambda}$ is the *round-trip* phase difference and the geometric series was used. Then the transmitted intensity will be

$$I_T = |E_T|^2 = |E_0|^2 \frac{|t|^4}{|1 - r^2 e^{i\delta}|^2} = I_0 \frac{T_0^2}{|1 - R^2 e^{i\delta}|^2} = I_0 \frac{T_0^2}{(1-R)^2} \cdot \frac{1}{1 + F \sin^2(\delta/2)}$$

where the Finesse is defined as:

$$F = \frac{4R}{(1-R)^2}$$

and any further phase shift introduced by the reflection coefficient r was included in $\delta = \frac{4\pi n d \cos\theta}{\lambda} + \phi$. The transmission will thus be:

$$T(\lambda) = \frac{I_T}{I_0} = \frac{1}{1 + F \sin^2(\delta/2)}$$

For small reflectivity $R \ll 1$ (plates are not intended to be mirrors in the first place) one gets $F \approx 4R \ll 1$ and:

$$\frac{1}{1 + F \sin(\delta/2)} \approx 1 - F \sin^2(\delta/2)$$

and using $\sin^2(\delta/2) = (1 - \cos\delta)/2$ the transmission can be rewritten as

$$T(\lambda) \approx 1 - F/2 + \frac{F}{2} \cdot \cos(\delta) = 1 - 2R + 2R \cdot \cos\left(\frac{4\pi n d \cos\theta}{\lambda} + \phi\right)$$

and the spectroscopic signal will be

$$S(\lambda) = S_0(\lambda)\left[C + A\cos\left(\frac{4\pi nd\cos\theta}{\lambda} + \phi\right)\right]$$

where A and C are respectively the amplitude and DC component of the modulation.

Calculation of the round-trip phase shift (see Figure A.1)

$$ac = 2l\sin\theta = 2\frac{d}{\cos\theta} = 2d\tan\theta$$

The Optical Path Difference between beams E_{01r} and E_{02r} is

$$OPD = n(ab+bc) - ac' = 2nl - ac\sin\theta_0 = 2n\frac{d}{\cos\theta} - 2d\tan\theta\sin\theta_0$$

but $n_0\sin\theta_0 = n\sin\theta$ thus $\sin\theta_0 = n\sin\theta$, thus

$$\begin{aligned} OPD &= 2n\frac{d}{\cos\theta} - 2d\tan\theta n\sin\theta = 2n\frac{d}{\cos\theta} - 2d\frac{\sin^2\theta}{\cos\theta} = \\ &= \frac{2nd}{\cos\theta}\left(1-\sin^2\theta\right) = \frac{2nd}{\cos\theta}\cos^2\theta = 2nd\cos\theta \end{aligned}$$

and the phase difference will be the optical path difference times the wavenumber:

$$\delta = k\cdot OPD = \frac{2\pi}{\lambda}\cdot 2nd\cos\theta = \frac{4\pi nd\cos\theta}{\lambda}$$

Bibliography

[1] N. F. Ramsey. «History of early atomic clocks.» In: *Metrologia* 42.3 (June 2005), S1–S3. ISSN: 1681-7575. DOI: 10.1088/0026-1394/42/3/s01 (cit. on p. 1).

[2] F. Riehle. *Frequency Standards: Basics and Applications*. Wiley, Sept. 2003. ISBN: 9783527605996. DOI: 10.1002/3527605991 (cit. on pp. 1, 5).

[3] A. Aeppli, K. Kim, W. Warfield, M. S. Safronova, and J. Ye. «Clock with 8×10−19 Systematic Uncertainty.» In: *Physical Review Letters* 133.2 (July 2024), p. 023401. ISSN: 1079-7114. DOI: 10.1103/physrevlett.133.023401 (cit. on p. 2).

[4] N. Dimarcq et al. «Roadmap towards the redefinition of the second.» In: *Metrologia* 61.1 (Jan. 2024), p. 012001. ISSN: 1681-7575. DOI: 10.1088/1681-7575/ad17d2 (cit. on p. 2).

[5] T. N. Bandi. «A Comprehensive Overview of Atomic Clocks and their Applications.» In: *Biology, Engineering, Medicine and Science Reports* 9.1 (Jan. 2023), pp. 01–10. ISSN: 2454-6895. DOI: 10.5530/bems.9.1.1 (cit. on p. 2).

[6] A. Strangfeld, S. Kanthak, M. Schiemangk, B. Wiegand, A. Wicht, A. Ling, and M. Krutzik. «Prototype of a compact rubidium-based optical frequency reference for operation on nanosatellites.» In: *Journal of the Optical Society of America B* 38.6 (May 2021), p. 1885. ISSN: 1520-8540. DOI: 10.1364/josab.420875 (cit. on p. 2).

[7] L. Maleki and J. Prestage. «Applications of clocks and frequency standards: from the routine to tests of fundamental models.» In: *Metrologia* 42.3 (June 2005), S145–S153. ISSN: 1681-7575. DOI: 10.1088/0026-1394/42/3/s15 (cit. on p. 2).

[8] M. Takamoto, I. Ushijima, N. Ohmae, T. Yahagi, K. Kokado, H. Shinkai, and H. Katori. «Test of general relativity by a pair of transportable optical lattice clocks.» In: *Nature Photonics* 14.7 (Apr. 2020), pp. 411–415. ISSN: 1749-4893. DOI: 10.1038/s41566-020-0619-8 (cit. on p. 2).

[9] B. White, R. Offer, A. Hilton, and A. Luiten. «The SWaP plot: Visualising the performance of portable atomic clocks as a function of their size, weight and power.» In: (Sept. 2024). DOI: 10.48550/ARXIV.2409.08484. arXiv: 2409.08484 [physics.atom-ph] (cit. on pp. 2, 3).

[10] A. C. Obaze-Adeleke, B. Semon, and T. N. Bandi. «A Comprehensive Review of Rubidium Two-Photon Vapor Cell Optical Clock: Long-Term Performance Limitations and Potential Improvements.» In: *Photonics* 12.5 (May 2025), p. 513. ISSN: 2304-6732. DOI: 10.3390/photonics12050513 (cit. on p. 2).

[11] B. L. S. Marlow and D. R. Scherer. «A Review of Commercial and Emerging Atomic Frequency Standards.» In: *IEEE Transactions on Ultrasonics, Ferroelectrics, and Frequency Control* 68.6 (June 2021), pp. 2007–2022. ISSN: 1525-8955. DOI: 10.1109/tuffc.2021.3049713 (cit. on p. 3).

[12] S. Knappe, V. Shah, P. D. D. Schwindt, L. Hollberg, J. Kitching, L.-A. Liew, and J. Moreland. «A microfabricated atomic clock.» In: *Applied Physics Letters* 85.9 (Aug. 2004), pp. 1460–1462. ISSN: 1077-3118. DOI: 10.1063/1.1787942 (cit. on pp. 3, 5, 20).

[13] M. Hasegawa, R. Chutani, C. Gorecki, R. Boudot, P. Dziuban, V. Giordano, S. Clatot, and L. Mauri. «Microfabrication of cesium vapor cells with buffer gas for MEMS atomic clocks.» In: *Sensors and Actuators A: Physical* 167.2 (June 2011), pp. 594–601. ISSN: 0924-4247. DOI: 10.1016/j.sna.2011.02.039 (cit. on pp. 3–5, 20).

[14] K. W. Martin et al. «Compact Optical Atomic Clock Based on a Two-Photon Transition in Rubidium.» In: *Physical Review Applied* 9.1 (Jan. 2018), p. 014019. ISSN: 2331-7019. DOI: 10.1103/physrevapplied.9.014019 (cit. on pp. 4, 6).

[15] Z. L. Newman, V. Maurice, C. Fredrick, T. Fortier, H. Leopardi, L. Hollberg, S. A. Diddams, J. Kitching, and M. T. Hummon. «High-performance, compact optical standard.» In: *Optics Letters* 46.18 (May 3, 2021), p. 4702. ISSN: 1539-4794. DOI: 10.1364/ol.435603. arXiv: 2105.00610 [physics.atom-ph] (cit. on pp. 4, 6).

[16] H. Jansen, M. De Boer, S. Unnikrishnan, M. Louwerse, and M. Elwenspoek. «Black silicon method: X. A review on high speed and selective plasma etching of silicon with profile control: an in-depth comparison between Bosch and cryostat DRIE processes as a roadmap to next generation equipment.» In: *Journal of Micromechanics and Microengineering* 19.3 (Feb. 2, 2009), p. 033001. DOI: 10.1088/0960-1317/19/3/033001 (cit. on pp. 4, 5, 26).

[17] F. Laermer and A. Urban. «Through-Silicon Vias Using Bosch DRIE Process Technology.» In: *Ultra-thin Chip Technology and Applications*. Springer New York, Nov. 12, 2010, pp. 81–91. DOI: 10.1007/978-1-4419-7276-7_9 (cit. on pp. 4, 5, 26).

[18] G. Wallis and D. I. Pomerantz. «Field Assisted Glass-Metal Sealing.» In: *Journal of Applied Physics* 40.10 (Sept. 1969), pp. 3946–3949. ISSN: 1089-7550. DOI: 10.1063/1.1657121 (cit. on pp. 4, 5, 32).

[19] L.-A. Liew, S. Knappe, J. Moreland, H. Robinson, L. Hollberg, and J. Kitching. «Microfabricated alkali atom vapor cells.» In: *Applied Physics Letters* 84.14 (Apr. 2004), pp. 2694–2696. ISSN: 1077-3118. DOI: 10.1063/1.1691490 (cit. on pp. 4, 5, 32).

[20] R. Chutani, M. Hasegawa, V. Maurice, N. Passilly, and C. Gorecki. «Single-step deep reactive ion etching of ultra-deep silicon cavities with smooth sidewalls.» In: *Sensors and Actuators A: Physical* 208 (Feb. 2014), pp. 66–72. ISSN: 0924-4247. DOI: 10.1016/j.sna.2013.12.031 (cit. on pp. 4, 5, 31).

[21] C. Carlé et al. «Reduction of helium permeation in microfabricated cells using aluminosilicate glass substrates and Al_2O_3 coatings.» In: *Journal of Applied Physics* 133.21 (Mar. 24, 2023). ISSN: 1089-7550. DOI: 10.1063/5.0151899. arXiv: 2303.13927 [physics.atom-ph] (cit. on pp. 4, 5, 32).

[22] J. Kitching. «Chip-scale atomic devices.» In: *Applied Physics Reviews* 5.3 (Sept. 2018), p. 031302. ISSN: 1931-9401. DOI: 10.1063/1.5026238 (cit. on p. 4).

[23] D. G. Bopp, V. M. Maurice, and J. E. Kitching. «Wafer-level fabrication of alkali vapor cells using in-situ atomic deposition.» In: *Journal of Physics: Photonics* 3.1 (Dec. 2020), p. 015002. ISSN: 2515-7647. DOI: 10.1088/2515-7647/abcbe5 (cit. on p. 5).

[24] B. Cagnac, G. Grynberg, and F. Biraben. «Spectroscopie d'absorption multiphotonique sans effet Doppler.» In: *Journal de Physique* 34.10 (1973), pp. 845–858. ISSN: 0302-0738. DOI: 10.1051/jphys:019730034010084500 (cit. on pp. 5, 13).

[25] G. Grynberg and B. Cagnac. «Doppler-free multiphotonic spectroscopy.» In: *Reports on Progress in Physics* 40.7 (July 1977), pp. 791–841. ISSN: 1361-6633. DOI: 10.1088/0034-4885/40/7/002 (cit. on pp. 5, 14).

[26] N. Jährling and S. Saghafi. «Ultramicroscopy – a novel light sheet based imaging technique created by various research disciplines.» In: *e & i Elektrotechnik und Informationstechnik* 128.10 (Oct. 2011), pp. 352–358. ISSN: 1613-7620. DOI: 10.1007/s00502-011-0045-1 (cit. on p. 8).

[27] B. E. A. Saleh and M. C. Teich. *Fundamentals of Photonics*. Wiley, Aug. 1991. ISBN: 9780471213741. DOI: 10.1002/0471213748 (cit. on p. 7).

[28] H. Kogelnik and T. Li. «Laser Beams and Resonators.» In: *Applied Optics* 5.10 (Oct. 1, 1966), p. 1550. DOI: 10.1364/ao.5.001550 (cit. on pp. 9, 51).

[29] C. Foot. *Atomic physics*. Oxford University Press, USA, 2005. URL: http://scholar.google.com/scholar.bib?q=info:RG8FFqhmF0kJ:scholar.google.com/&output=citation&hl=en&ct=citation&cd=0 (cit. on p. 10).

[30] E. Arimondo, M. Inguscio, and P. Violino. «Experimental determinations of the hyperfine structure in the alkali atoms.» In: *Reviews of Modern Physics* 49.1 (Jan. 1977), pp. 31–75. ISSN: 0034-6861. DOI: 10.1103/revmodphys.49.31 (cit. on p. 13).

[31] S. Bize, Y. Sortais, M. S. Santos, C. Mandache, A. Clairon, and C. Salomon. «High-accuracy measurement of the 87 Rb ground-state hyperfine splitting in an atomic fountain.» In: *Europhysics Letters (EPL)* 45.5 (Mar. 1999), pp. 558–564. ISSN: 1286-4854. DOI: 10.1209/epl/i1999-00203-9 (cit. on p. 13).

[32] J. Ye, S. Swartz, P. Jungner, and J. L. Hall. «Hyperfine structure and absolute frequency of the ^{87}Rb $5P_{3/2}$ state.» In: *Optics Letters* 21.16 (Aug. 1996), p. 1280. ISSN: 1539-4794. DOI: 10.1364/ol.21.001280 (cit. on p. 13).

[33] M. P. Bradley, J. V. Porto, S. Rainville, J. K. Thompson, and D. E. Pritchard. «Penning Trap Measurements of the Masses ofC133s,R87,85b, andN23awith Uncertainties $\leq$ 0.2ppb.» In: *Physical Review Letters* 83.22 (Nov. 1999), pp. 4510–4513. ISSN: 1079-7114. DOI: 10.1103/physrevlett.83.4510 (cit. on p. 13).

[34] R. F. Gutterres, C. Amiot, A. Fioretti, C. Gabbanini, M. Mazzoni, and O. Dulieu. «Determination of the 87Rb 5p state dipole matrix element and radiative lifetime from the photoassociation spectroscopy of the Rb 2 0 g-(P3/2) long-range state.» In: *Physical Review A* 66.2 (Aug. 2002), p. 024502. ISSN: 1094-1622. DOI: 10.1103/physreva.66.024502 (cit. on p. 13).

[35] F. Nez, F. Biraben, R. Felder, and Y. Millerioux. «Optical frequency determination of the hyperfine components of the two-photon transitions in rubidium.» In: *Optics Communications* 102.5-6 (Oct. 1993), pp. 432–438. ISSN: 0030-4018. DOI: 10.1016/0030-4018(93)90417-4 (cit. on pp. 13, 16).

[36] M. Göppert-mayer. «Über Elementarakte mit zwei Quantensprüngen.» In: *Annalen der Physik* 401.3 (Jan. 1931), pp. 273–294. DOI: 10.1002/andp.19314010303 (cit. on p. 13).

[37] I. Abella. «Optical Double-Photon Absorption in Cesium Vapor.» In: *Physical Review Letters* 9.11 (Dec. 1, 1962), pp. 453–455. DOI: 10.1103/physrevlett.9.453 (cit. on p. 13).

[38] L. S. Vasilenko, V. P. Chebotaev, and A. V. Shishaev. «Line Shape of Two-Photon Absorption in a Standing-Wave Field in a Gas.» In: *Soviet Journal of Experimental and Theoretical Physics Letters* 12 (Jan. 1970), p. 113 (cit. on p. 13).

[39] F. Biraben. «The first decades of Doppler-free two-photon spectroscopy.» In: *Comptes Rendus. Physique* 20.7-8 (May 2019), pp. 671–681. ISSN: 1878-1535. DOI: 10.1016/j.crhy.2019.04.003 (cit. on p. 15).

[40] U. Volz and H. Schmoranzer. «Precision lifetime measurements on alkali atoms and on helium by beam-gas-laser spectroscopy.» In: *Physica Scripta* T65 (Jan. 1996), pp. 48–56. ISSN: 1402-4896. DOI: 10.1088/0031-8949/1996/t65/007 (cit. on pp. 16, 19, 60).

[41] E. J. Ahern, S. K. Scholten, C. Locke, N. Bourbeau-Hebert, B. White, A. N. Luiten, and C. Perrella. «Tailoring the Stability of a Two-Color, Two-Photon Rubidium Frequency Standard.» In: *Phys. Rev. Applied 23, 044025 (2025)* 23.4 (Oct. 22, 2024), p. 044025. ISSN: 2331-7019. DOI: 10.1103/physrevapplied.23.044025. arXiv: 2410.16654 [physics.atom-ph] (cit. on p. 16).

[42] R. Beard, K. W. Martin, J. D. Elgin, B. L. Kasch, and S. P. Krzyzewski. «Two-photon rubidium clock detecting 776 nm fluorescence.» In: *Optics Express* 32.5 (Feb. 2024), p. 7417. ISSN: 1094-4087. DOI: 10.1364/oe.513974 (cit. on p. 16).

[43] W. Demtroeder. *Laser Spectroscopy*. Springer Berlin Heidelberg, 2003. DOI: 10.1007/978-3-662-05155-9 (cit. on pp. 16, 38).

[44] B. L. Keliehor. «Technology development for a compact rubidium optical frequency reference.» PhD thesis. 2023. DOI: 10.48730/Z5QE-D927 (cit. on p. 17).

[45] F. Biraben, M. Bassini, and B. Cagnac. «Line-shapes in Doppler-free two-photon spectroscopy. The effect of finite transit time.» In: *Journal de Physique* 40.5 (1979), pp. 445–455. ISSN: 0302-0738. DOI: 10.1051/jphys:01979004005044500 (cit. on p. 18).

[46] N. D. Zameroski, G. D. Hager, C. J. Erickson, and J. H. Burke. «Pressure broadening and frequency shift of the 5S1/2→ 5D5/2and 5S1/2→ 7S1/2two photon transitions in85Rb by the noble gases and N2.» In: *Journal of Physics B: Atomic, Molecular and Optical Physics* 47.22 (Oct. 2014), p. 225205. ISSN: 1361-6455. DOI: 10.1088/0953-4075/47/22/225205 (cit. on p. 19).

[47] H. Seidel, L. Csepregi, A. Heuberger, and H. Baumgärtel. «Anisotropic Etching of Crystalline Silicon in Alkaline Solutions: I . Orientation Dependence and Behavior of Passivation Layers.» In: *Journal of The Electrochemical Society* 137.11 (Nov. 1990), pp. 3612–3626. ISSN: 1945-7111. DOI: 10.1149/1.2086277 (cit. on p. 31).

[48] W. Kern. «The Evolution of Silicon Wafer Cleaning Technology.» In: *Journal of The Electrochemical Society* 137.6 (June 1990), pp. 1887–1892. ISSN: 1945-7111. DOI: 10.1149/1.2086825 (cit. on p. 31).

[49] S. Cheng. «On the mechanism of helium permeation through silica glass.» In: *AIMS Materials Science* 11.3 (2024), pp. 438–448. ISSN: 2372-0484. DOI: 10.3934/matersci.2024022 (cit. on p. 32).

[50] B. Michel and H. Reichl, eds. *The world of electronic packaging and system integration. Anniversary edition 60th birthday of Herbert Reichl*. Literaturangaben. Dresden: Ddp Goldenbogen-Verl., 2004. 605 pp. ISBN: 3932434765 (cit. on p. 32).

[51] G. Wallis. «Field Assisted Glass Sealing.» In: *Active and Passive Electronic Components* 2.1 (Jan. 1975), pp. 45–53. ISSN: 1563-5031. DOI: 10.1155/apec.2.45 (cit. on p. 33).

[52] P. Knapkiewicz. «Technological Assessment of MEMS Alkali Vapor Cells for Atomic References.» In: *Micromachines* 10.1 (Dec. 2018), p. 25. ISSN: 2072-666X. DOI: 10.3390/mi10010025 (cit. on p. 37).

[53] M. Gozzelino, E. Cerrato, C. Gionco, S. Micalizio, G. Aprile, M. Crivellari, F. Levi, and D. Calonico. «Activation and characterization of Rb MEMS cells with an automatic system at wafer level.» In: *Sensors and Actuators A: Physical* 391 (Sept. 2025), p. 116621. ISSN: 0924-4247. DOI: 10.1016/j.sna.2025.116621 (cit. on pp. 38, 39).

[54] G. Ghione. *Semiconductor Devices for High-Speed Optoelectronics*. Cambridge University Press, Oct. 2009. ISBN: 9780511635595. DOI: 10.1017/cbo9780511635595 (cit. on pp. 39, 47).

[55] G. R. Fowles. *Introduction to modern optics*. 2. ed., corr. republication. Unabridged, corrected republication of the 2. ed., New York, 1975. New York: Dover Publications, 1989. 328 pp. ISBN: 9780486659572 (cit. on p. 41).

[56] C. B. Alcock, V. P. Itkin, and M. K. Horrigan. «Vapour Pressure Equations for the Metallic Elements: 298–2500K.» In: *Canadian Metallurgical Quarterly* 23.3 (July 1984), pp. 309–313. ISSN: 1879-1395. DOI: 10.1179/cmq.1984.23.3.309 (cit. on p. 45).

[57] P. Siddons, C. S. Adams, C. Ge, and I. G. Hughes. «Absolute absorption on rubidium D lines: comparison between theory and experiment.» In: *Journal of Physics B: Atomic, Molecular and Optical Physics* 41.15 (July 2008), p. 155004. ISSN: 1361-6455. DOI: 10.1088/0953-4075/41/15/155004 (cit. on p. 46).

[58] J. E. Sansonetti and W. C. Martin. «Handbook of Basic Atomic Spectroscopic Data.» In: *Journal of Physical and Chemical Reference Data* 34.4 (Sept. 2005), pp. 1559–2259. ISSN: 1529-7845. DOI: 10.1063/1.1800011 (cit. on p. 60).